Advances in Polymer Technology

Designing and Manufacturing of Stimuli-Responsive Polymeric Materials

Lead Guest Editor: Hao Sun
Guest Editors: Zhao Wang and Xiaosong Cao

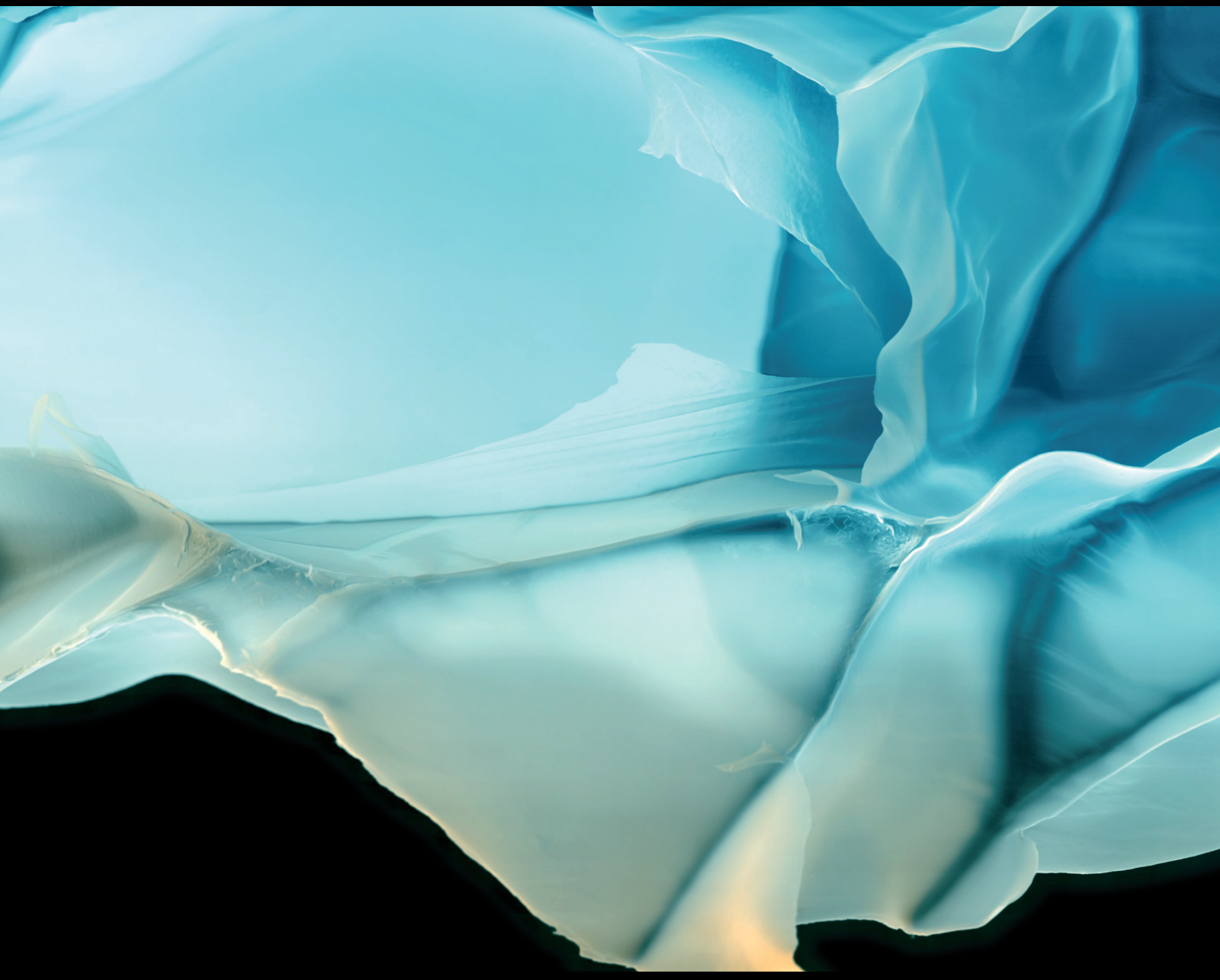

Designing and Manufacturing of Stimuli-Responsive Polymeric Materials

Advances in Polymer Technology

Designing and Manufacturing of Stimuli-Responsive Polymeric Materials

Lead Guest Editor: Hao Sun
Guest Editors: Zhao Wang and Xiaosong Cao

Contents

Hindawi
Advances in Polymer Technology
Volume 2020, Article ID 3927860, 10 pages
https://doi.org/10.1155/2020/3927860

Research Article

Facile Fabrication of Composite Scaffolds for Long-Term Controlled Dual Drug Release

Dawei Li,[1] Chao Li,[1] Xing Wang ,[2,3] Chunlin Li,[1] Tunan Sun,[1] Jin Zhou ,[1] and Gang Li [1]

[1]*The 8th Medical Center of Chinese, PLA General Hospital, Beijing 100091, China*
[2]*Beijing National Laboratory for Molecular Sciences, State Key Laboratory of Polymer Physics & Chemistry, Institute of Chemistry, Chinese Academy of Sciences, Beijing 100190, China*
[3]*University of Chinese Academy of Sciences, Beijing 100049, China*

Correspondence should be addressed to Xing Wang; wangxing@iccas.ac.cn, Jin Zhou; huoshan1975@sina.com, and Gang Li; ligamg@sina.com

Received 14 June 2019; Accepted 12 September 2019; Published 5 January 2020

Guest Editor: Xiaosong Cao

Bone tuberculosis (TB) caused by mycobacterium tuberculosis continues to present a formidable challenge to humans. To effectively cure serious bone TB, a novel kind of composite scaffolds with long-term dual drug release behaviours were prepared to satisfy the needs of both bone regeneration and antituberculosis drug therapy. In virtue of an improved O/W emulsion technique, water-soluble isoniazid (INH)-loaded gelatin microparticles were obtained by tailoring the content of β-tricalcium phosphate (β-TCP), which played significant roles in INH entrapment efficiency and drug release behaviours. By mixing with the poly(ε-caprolactone)-*block*-poly (lactic-*co*-glycolic acid) (*b*-PLGC) solution containing oil-soluble rifampicin (RFP) via the particle leaching combined with phase separation technique, the dual drugs-loaded composite scaffolds were fabricated, which possessed interconnected porous structures and achieved the steady release of INH and RFP drugs for three months. Moreover, this dual drugs-loaded system could basically achieve their expectant roles of respective drugs without obvious influences with each other. This strategy on preparation of intelligent composite scaffolds with the multi-drugs loading capacity and controlled long-term release behaviour will be potential and promising substrates in clinical treatment of bone tuberculosis.

1. Introduction

Bacterial infections are one of the most common diseases threatening the human health, which have resulted in the severe illness to destroy the infected tissues, such as bone tuberculosis (TB) and osteomyelitis [1–4]. Traditional therapy of the infections mainly includes the disinfection/bacteriostasis and reparation of the destroyed tissues. Take serious bone TB for instance, the standard course involves a more-than-6-months medication treatment to inhibit bacteria and a bone implantation after the lesion removed operation to fill and repair the cavities. A local drug delivery system (DDS) offers an effective approach for the drug therapy of bone TB. It possesses advantages of specific site delivery, drug dosage optimization and release duration. Therefore, DDS technology is recognized as the best candidate for achieving the drug therapy while tissue engineering is the most prospective method for the defect reparation [5–9]. It follows that the combination of DDS and tissue engineering should be a natural way to simultaneously satisfy the two aspects of bone TB therapy.

Recently, many researchers have been focusing on this feasible strategy. For example, Huang's groups and Kang's groups had utilized a chemical bonding technique to conjugate the drugs to biodegradable polymers to gain the tissue engineering scaffolds respectively, which could implement the prolonged drug release and satisfactory tissue regeneration. However, the chemical bonding technique always carried out a long-term drug release (about 6 months) with a slightly initial burst release. In addition, it had inevitable defectiveness of the possible drug degeneration and incomplete drug release, in particular the possible change in pharmacological effects after chemical bonding and during degradation of the polymer. When its molecular weight is lower than 5000, the degraded fragment of polylactone linked with a drug molecule can be dissolved in water and is considered as a drug molecule, but whether it can play the same role as a drug molecule is

doubtful. As a result, the physical blending technique was more preferable for achieving the controlled drug release from scaffolds [10–14]. Then, a newly designed polylactone of *b*-PLGC was adopted to produce a bone tissue-engineered scaffold with capability of elongating the drug release time to 98 days and reducing the initial burst release to lower than 40%. Nevertheless, it was mostly reported that with similar physical blending technique the release time could only last less than 50 days and the initial burst release reached up to higher than 60% [15]. In spite of technical differences, the above-mentioned works can meet the demands of both reparative and bacteriostatic functions. Nonetheless, the constant release of only one drug in the focus of infection may lead to the drug-resistance of bacteria; in this case, it is urgent to adopt the multiple drugs for local therapy in clinical practice [16, 17]. Therefore, establishment of long-term multiple drug release system is a correct direction to move forward not only in this research but in clinical area.

In addition to the first-line antituberculosis drugs such as isoniazid (INH), rifampicin (RFP), pyrazinamide and ethambutol, others like p-aminosalicylic acid, ethionamide, protionamide and cycloserine are also included for the multiple-drugs therapy of bone TB [18–23]. These drugs can be classified by solubility into two categories of water-soluble and oil-soluble. For the purpose of simplifying the laboratory model, one typical drug from each category was picked out to be loaded in tissue engineering scaffolds at the same time. Considering the clinically wide usage, INH was the suitable representative of water-soluble drugs and RFP was that of oil-soluble drugs. It was easy to load RFP into the tissue engineering scaffolds by the physical blending technique because the oil-soluble RFP could dissolve well in organic solvents and disperse evenly in the polylactone scaffold. Oppositely, the loading of INH was difficult. The phase separation of INH and polylactone may result in an uneven INH distribution. In addition, the water-solubility of INH demands a non-aqueous washing process to avoid uncontrolled loss, but most commonly, tissue-engineering scaffolds fabricating technique was solution cast/porogen leaching, in which the inorganic salts (mostly NaCl particles) were adopted as porogen while the water was a necessity during leaching process [24–26]. To circumvent this problem, gelatin coating and crosslinking techniques were taken to load INH into TCP nanoparticles. Under this circumstance, the particles could be carried into polylactone/TCP composite scaffolds with little INH loss after porogen leaching process.

In this work, we incorporated the TCP nanoparticles into the RFP-containing PLGC polymer matrix to form the composite scaffolds. Since PCL has high permeability for drug molecules and PLGA has flexibility in degradation adjustment, the RFP-releasing behavior and degradation rate of scaffolds were mainly controlled by the degradation and drug permeability of *b*-PLGC polymer, which could effectively improve the uniformity, extend the release duration and suppress the initial burst release. Furthermore, by means of the complicated physical blending technique, the water-soluble INH drug was also encapsulated into the composite scaffolds to yield a novel kind of dual anti-tuberculosis drug-loaded composite scaffold and realize a controllably prolonged local drug delivery. Using this principle, many sophisticated scaffold materials with the multiple loading and tailored releases of drugs may have great applications in bone TB therapy.

2. Materials and Methods

2.1. Materials. Lactide and glycolide were purchased from Purac (Netherlands) and purified by recrystallization in ethyl acetate twice. ε-caprolactone was purchased from Acros Chemica (Belgium), dried with calcium hydride for 24 h, and distilled under vacuum (82°C /133 Pa). Stannous octoate (analytical grade) and isoniazid (INH, 99%) were purchased from Sigma-Aldrich. RFP was purchased from Energy Chemical, China. β-tricalcium phosphate (β-TCP) powder with diameter of 300–500 nm was purchased from the Forth Reagent Factory of Shanghai, China. Ethyl acetate was dried by P_2O_5 overnight and then distilled. NaCl of analytical quality was purchased from Beijing Chemical Works, China. It was sieved and particles with diameter of 150–300 μm were selected. Gelatin (analytical grade), solvents and other compounds were obtained from Beijing Chemical Reagents Company, China. All reagents were used as received unless otherwise noted.

2.2. Characterizations. ^{1}H NMR spectra was obtained on a Bruker DRX-400 spectrometer in chloroform-d using tetramethylsilane (TMS) as an internal reference. Gel permeation chromatography (GPC) measurements were carried out on VE-2001 (Viscotek, UK) maintained at 35°C using chloroform as eluent at a flow rate of 1.0 mL/min. Scanning electron microscopy (SEM) images were obtained at acceleration voltage of 5 kV on a JSM-6700F microscope (JEOL, Japan). The samples were sputter-coated with a thin layer of Pt for 120 s to make the samples conductive before testing. Thermogravimetric analysis (TGA) measurements were performed on a TA Instruments, Inc., MDSC-2910. The temperature program was from 30 to 700°C with an increasing rate of 10°C min^{-1} in a flow of air. UV–vis spectra were measured on a Hitachi U-3010 spectrometer and fluorescence measurements were carried out on a Hitachi F4600 photoluminescence spectrometer with a xenon lamp as a light source. Confocal laser scanning microscopy (CLSM, Zeiss LSM 510, Germany) was under excitation at 314 nm.

2.3. Preparation and Characterization of b-PLGC. According to our previous report, poly(ε-caprolactone)-*block*-poly(lactic-*co*-glycolic acid) (*b*-PLGC) copolymer was synthesized via two steps [15]. Firstly, the PCL pre-polymer was prepared by ring-opening polymerization of ε-caprolactone (CL) under 65 Pa in sealed glass ampoules at 140°C for 20 h in the presence of hexadecanol as initiator and stannous octoate as catalyst (0.05 wt%). Subsequently, purified PCL pre-polymer, glycolide, lactide, and stannous octoate were sealed into a deoxygenating glass tube under vacuum at 160°C for 20 h. After that, the raw product was dissolved in chloroform, precipitated into ethanol and then dried thoroughly under vacuum for 48 h.

2.4. Preparation and Characterization of Gelatin INH-Loaded Particles. INH-loaded Gelatin particles were prepared via a

modified O/W emulsion technique [27]. Firstly, INH solution with concentration of 10 wt% was made by dissolving INH in deionized water. Then a certain amount of TCP nanoparticles were added into. After the TCP nanoparticles were evenly dispersed, 1.0 g of gelatin was put into the 10 mL of INH solution containing TCP nanoparticles. The solution was heated to 45°C as the water phase, which was slowly added to the 350 mL of soybean oil containing the 0.675 g of span 80 as oil phase with stirring speed of 200 rpm. 10 minutes later, the stirring speed was raised up to 400 rpm and further kept for 30 min while the system was naturally cooling down to room temperature. After that, the product was washed by acetone for 4 times and isopropanol for 3 times. Next, the obtained microparticles were freeze-dried for 48 h and then crosslinked by the glutaraldehyde dissolved in 100 mL of acetone. Afterwards, the particles were added into 300 mL of solution with 10 mmol glycine and 0.1 wt% span 80 to remove the residual glutaraldehyde. At last, the microparticles were washed by water for 3 times. After the freeze-dried process for 48 h, the final samples were sealed and kept in a 4°C refrigerator. The microparticles with theoretical TCP content of 0 wt%, 33 wt% and 50 wt% were abbreviated as INH@GMs, INH-TCP@GMs3367 and INH-TCP@GMs5050, respectively.

After the microparticles were coated with platinum using a sputter coater (E-1010, Hitachi Ltd, Japan), their morphology was observed by SEM (JSM-6700F, JEOL Ltd, Japan). The average diameter was calculated by measuring 5 SEM pictures of each sample with more than 100 particles on every picture measured. TCP content was measured by TGA (Pyris 1, PerkinElmer, USA) with a temperature range of 30–700°C and a temperature rise speed of 10°C/min.

2.5. Preparation and Characterization of Composite Scaffolds. Based on our previous study, the composite scaffolds were fabricated by particle leaching combined with phase separation techniques [15, 24, 25]. The b-PLGC scaffolds loaded with INH-TCP@GMs and RFP were prepared as follows: Firstly, b-PLGC, RFP and 1,4-dioxane in the proportion of 5: 1: 90 (wt. ratio) were stirred for 24 h to form a solution. Then a certain quality of INH-TCP@GMs5050 and pre-sieved NaCl particles with a weight ratio of 40/1 to *b*-PLGC were added into the solution and stirred vigorously to form a slurry mixture. Next, the slurry was fitted into a mold, frozen under −20°C and freeze-dried for 48 h. After a complete rinse with distilled water and a subsequent 24 h freeze-drying, the PLGC scaffolds loaded with INH and RFP was obtained. The content of INH-TCP@GMs5050 in the obtained scaffolds were 50 wt% so these scaffolds were abbreviated as I-M/RP50.

The *b*-PLGC scaffolds loaded with INH-TCP@GMs was prepared similarly, and the only difference was that no RFP was introduced in the *b*-PLGC solution. The contents of INH-TCP@GMs5050 in the scaffolds were 50 wt% and 70 wt%, so these scaffolds were marked as I-M/P50 and I-M/P70, respectively.

The b-PLGC scaffolds loaded with INH and without INH-TCP@GMs were prepared likewise, and the only difference was that TCP nanoparticles and INH were respectively added into the *b*-PLGC solution directly to take the place of INH-TCP@GMs5050. The INH-loaded *b*-PLGC scaffold without INH-TCP@GMs was named as INH/TCP/*b*-PLGC for short. After the scaffolds were coated with platinum using a sputter coater, their morphology was characterized by SEM. The scaffolds carrying gelatin particles loaded with Evans blue and TCP were cut into slices and observed under a confocal laser scanning microscopy (CLSM, Zeiss LSM 510, Germany) at 540 nm. Pore size was measured using the ImageJ software (National Institutes of Health, USA) according to the SEM micrographs. For each scaffold, the average diameter of the pores was calculated based on 100 measurements. The porosity of the scaffolds was determined as described previously [28]. TCP content of scaffolds was measured by TGA (Pyris 1, PerkinElmer, USA) with a temperature range of 30–700°C and a temperature rise speed of 10°C/min.

2.6. INH Loading Content and Entrapment Efficiency of Gelatin Particles. INH Loading content and entrapment efficiency of gelatin particles were confirmed by extraction method. Firstly, a standard curve was gained by a series of INH concentrations in PBS using a UV spectrophotometer (TU-1901, PERSEE, China) at $\lambda_{max} = 263$ nm. Then 10 mg of INH-loaded particles was added into NaOH solution and the solution was heated to 60°C for 2 h to dissolve particles completely. Next, hydrochloric acid was put in to neutralize the alkalinity and dilute PBS to 5 mL. After that, the solution was centrifuged at 8000 rpm for 10 min to remove the TCP particles and acquire clear solution, which was analyzed using a UV spectrophotometer at $\lambda_{max} = 263$ nm. Meanwhile, the same quality of pure particles without INH was treated in the same way as the INH-loaded particles and the clear solution obtained were served as a control. The INH concentration was calculated through a calibration curve gained from INH standard solutions at different concentrations. The percentages of INH loading and encapsulation efficiency were calculated as follows:

$$\text{INH loading content } (\%) = \frac{(\text{Weight of INH in particle})}{(\text{Weight of INH-loaded particle}) \times 100\%}, \quad (1)$$

$$\text{INH entrapment efficiency } (\%) = \frac{(\text{Weight of INH in particle})}{(\text{Weight of INH feeding}) \times 100\%}. \quad (2)$$

2.7. INH Release Behaviours of Particles. In vitro release behaviours of INH@GMs, INH-TCP@GMs3367 and INH-TCP@GMs5050 were carried out at 37°C in 10 mL of 0.1 M PBS (pH = 7.4), respectively. The release medium was withdrawn at pre-determined time intervals and replaced with fresh PBS each time. Then the INH was determined by the UV spectrophotometer at $\lambda_{max} = 263$ nm. The concentration of INH was calculated with a calibration curve from INH standard solutions at different concentrations.

2.8. Drug Release Behaviours of Various Scaffolds. In vitro release behaviours of various scaffolds were performed at 37°C in 10 mL of 0.1 M PBS (pH = 7.4), respectively. The release medium was taken away at pre-set time intervals and displaced with fresh PBS each time. Then the INH and RFP were determined by UV spectrophotometer at $\lambda_{max} = 263$ nm

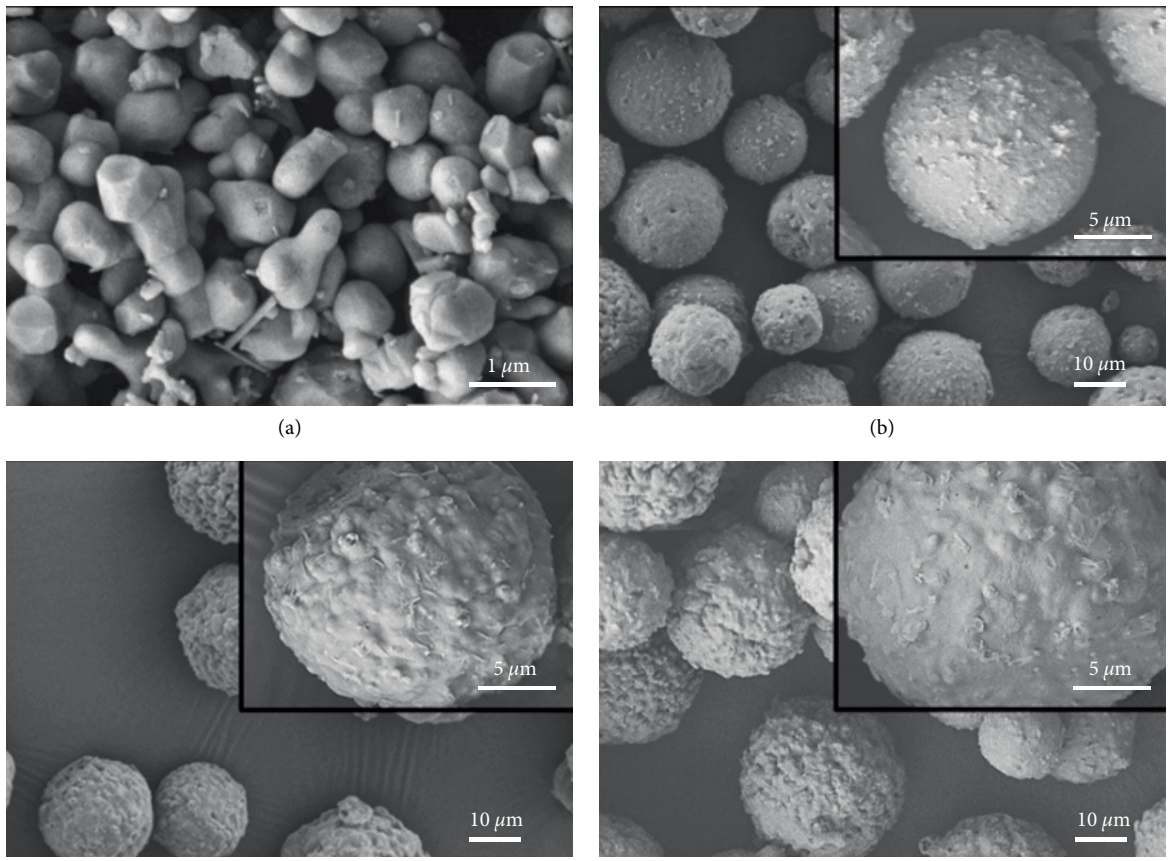

Figure 1: SEM images showing the TCP and INH-loaded gelation microparticles of (a) TCP, (b) INH@GMs, (c) INH-TCP@GMs3367 and (d) INH-TCP@GMs5050.

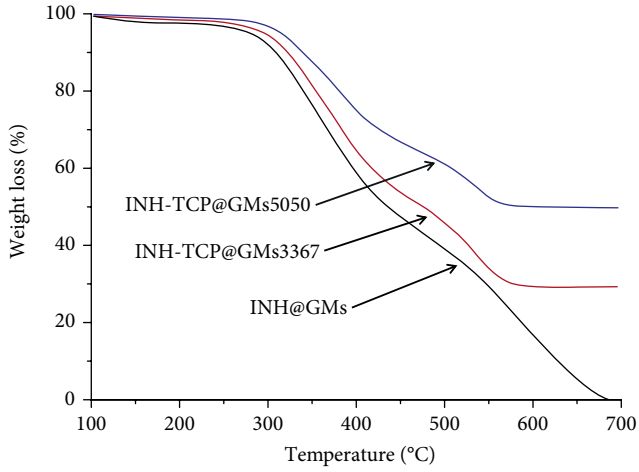

Figure 2: TGA curves of various INH-loaded microparticles.

and 474 nm, respectively. The contents of INH and RFP were calculated with the calibration curve from INH and RFP standard solutions at different concentrations.

2.9. Statistical Analysis. All quantitative data were expressed as mean ± standard deviation ($n = 3$). Statistical analysis was made based on t-test and the differences.

Table 1: INH loading content and entrapment efficiency of GMs and TCP@GMs microparticles.

Parameters	GMs	Microparticles TCP@ GMs3367	TCP@ GMs5050
INH loading content (wt%)[a]	3.7 ± 0.2	4.5 ± 0.3	5.0 ± 0.5
Entrapment efficiency (%)	37.0 ± 2.0	45 ± 3.0	50 ± 5.0

[a]Feeding dose of INH to (TCP + GM) in GMs and TCP@GMs microparticles was 10 : 90.

3. Results and Discussion

3.1. Fabrication of b-PLGC Scaffolds Loaded with INH and RFP

3.1.1. Preparation and Characterization of the INH-Loaded Gelatin Microparticles. The morphology of INH-loaded gelatin microspheres was prepared by the modified O/W emulsion technique. As shown in Figure 1, SEM images showed the particle size of TCP with a range of 300–500 nm while the size of INH-loaded gelatin particles was 10–30 μm. As the increase of TCP content, the particle sizes of INH@GMs, INH-TCP@GMs3367 and INH-TCP@GMs5050 were

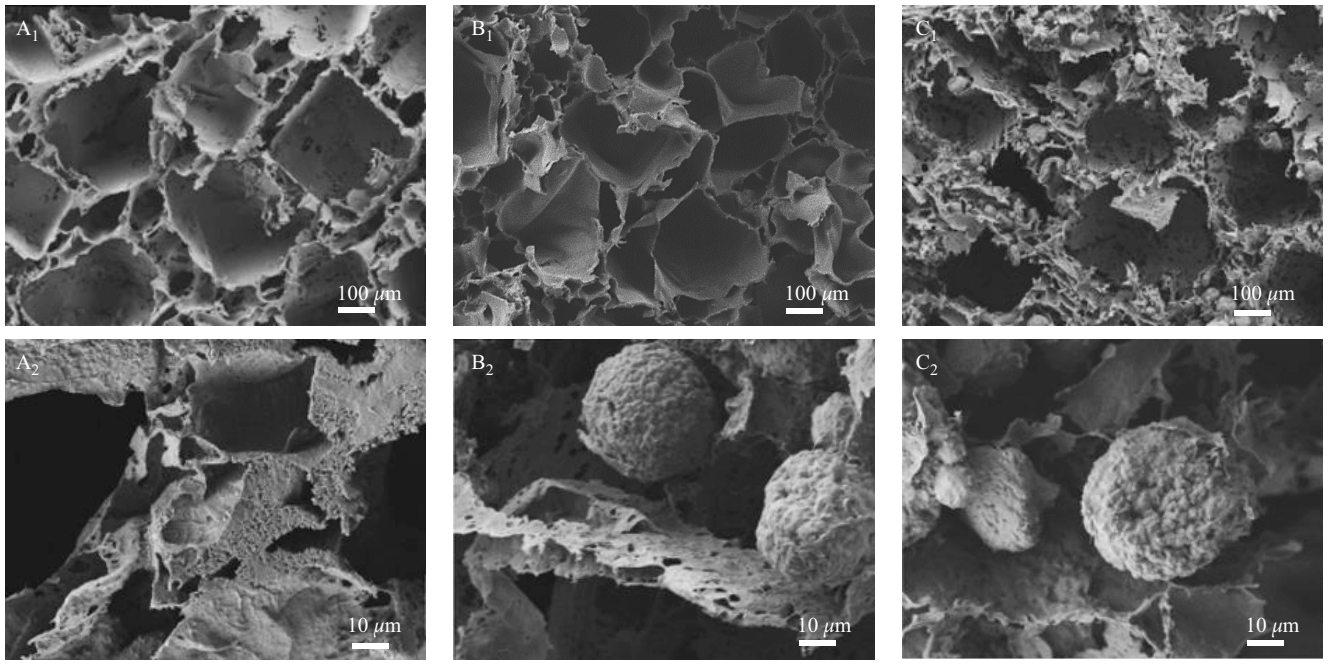

Figure 3: SEM images showing the INH-loaded *b-PLGC* scaffolds with different contents of microparticles. (a) INH/TCP/*b*-PLGC scaffolds; (b) I-M/P50 scaffolds and (c) I-M/P70 scaffolds.

Table 2: Pore parameters of INH-loaded *b*-PLGC scaffolds with different contents of microparticles.

Parameters	Scaffolds		
	INH/TCP/*b*-PLGC	I-M/P50	I-M/P70
Average pore diameter (μm)	253.0 ± 34.0	234.0 ± 39.0	231.0 ± 27.0
Porosity (%)	87.6 ± 1.5	84.5 ± 2.1	83.8 ± 1.4

17.2 ± 2.1 μm, 21.8 ± 1.9 μm and 23.1 ± 2.4 μm obtained from ImageJ software, respectively.

The TCP content in the microparticles was measured by thermogravimetric analysis (TGA) as showed in Figure 2. The quantities of INH@GMs, INH-TCP@GMs3367 and INH-TCP@GMs5050 were 0 wt%, 29.3 wt% and 50.0 wt% respectively, which were conformed to their theoretical contents, indicating the minimal loss of TCP in the preparation of microparticles.

As shown in Table 1, the INH loading content and entrapment efficiency of various microparticles were ranged from 3.7% to 5.0% and 37% to 50%, respectively. When the TCP content was increased, the INH loading content and entrapment efficiency grew correspondingly, which was attributed to the relatively large surface area of TCP that possessed a certain drug absorption effect. However, there was still a part of the drug loss during the microparticles preparing process due to mechanical agitation and slight solubility of INH in acetone. The above results manifested the successful preparation of the INH-loaded gelatin microparticles.

3.1. 2. Preparation and Characterization of b-PLGC Scaffolds Loaded with INH-TCP@GMs and RFP. The *b*-PLGC scaffolds loaded with INH-TCP@GMs were fabricated by particle leaching combined with phase separation technique. The morphology of scaffolds was determined by SEM observation and compared with the *b*-PLGC scaffolds loaded INH without microparticles, as shown in Figure 3. The pore size of the scaffolds loaded with INH-TCP@GMs was in a range of 200–300 μm. Similar with the INH/TCP/*b*-PLGC scaffolds, numerous micro-pores (10–50 μm) could be seen on the wall of macro-pores. The results manifested that the microparticles did not affect the characterization of scaffolds, which could provide a high surface area for the cell seeding, attachment and proliferation, deliver nutrient and elimination of metabolized products [29–32].

The pore size and porosity of scaffolds were also acquired respectively by dint of ImageJ software and volume exclusive method as shown in Table 2. The pore sizes of I-M/P50 and I-M/P70 scaffolds were in the range of 200–300 μm while the porosity was above 80%. These results pointed out that the pore size and porosity of scaffolds were slightly decreased after incorporating the INH-TCP@GMs.

To further analyze the distribution of microparticles, a water-soluble fluorescent polymer, Evans blue, was loaded on the microparticles instead of INH. The formed composite scaffolds, described as E-M/P50 and E-M/P70, were analyzed by the confocal laser scanning in Figure 4. The results showed that these microparticles were distributed throughout these scaffolds with a relative uniformity, e.g. some particles spread at the junction of different pores and others were embedded in the inner of scaffolds.

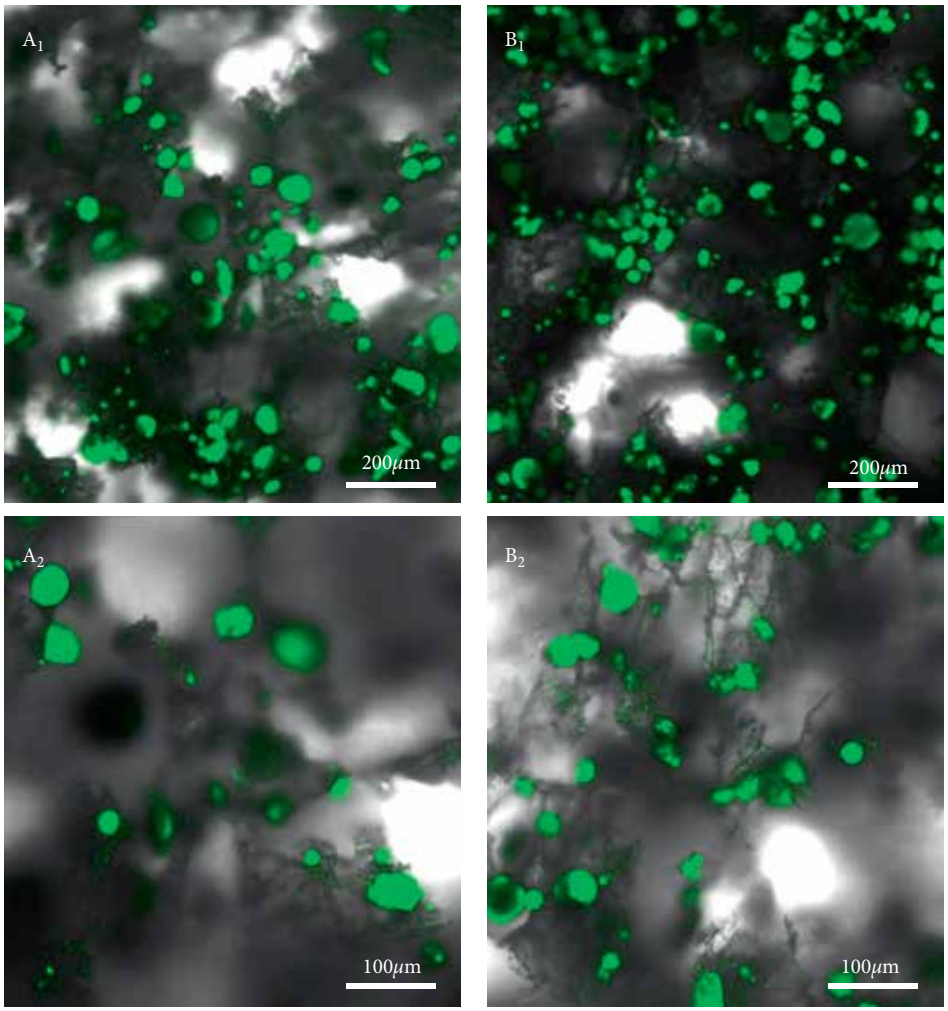

Figure 4: CLSM images of Evans blue loaded TCP@GMs/*b*-PLGC scaffolds of (a) E-M/P50 and (b) E-M/P70.

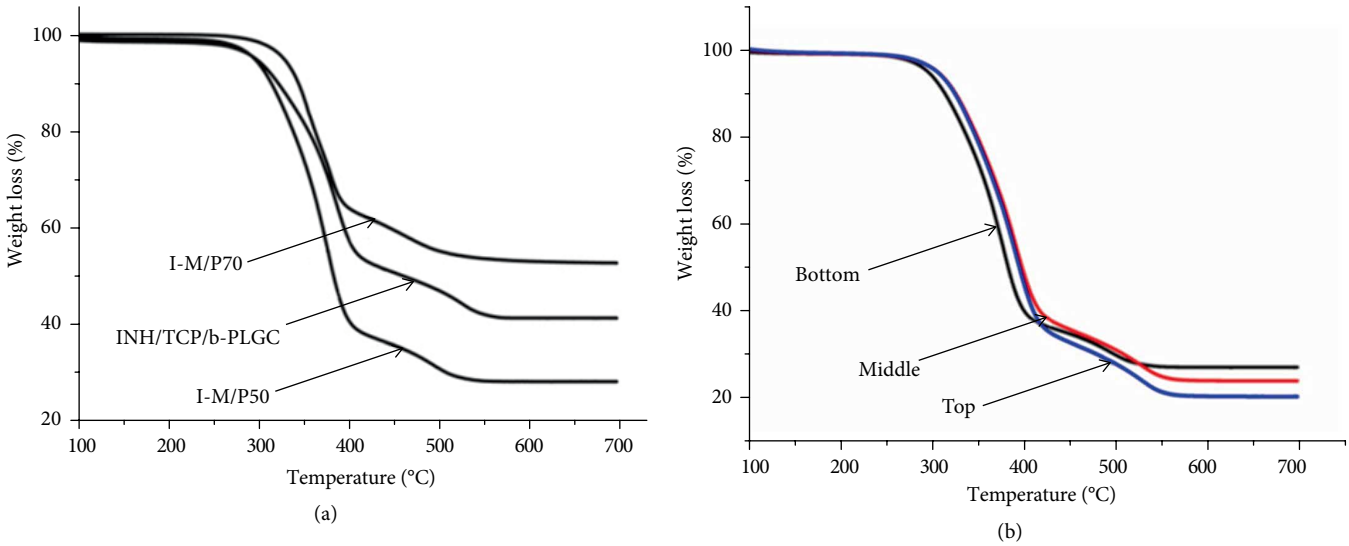

Figure 5: TGA curves of INH-loaded *b*-PLGC scaffolds with (a) different content of microparticles and (b) different parts of I-M/P50 scaffolds.

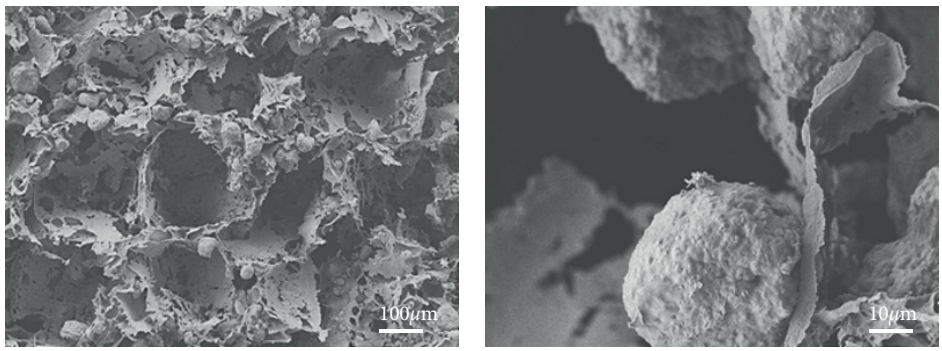

(a) (b)

Figure 6: Morphologies of I-M/RP50 scaffolds.

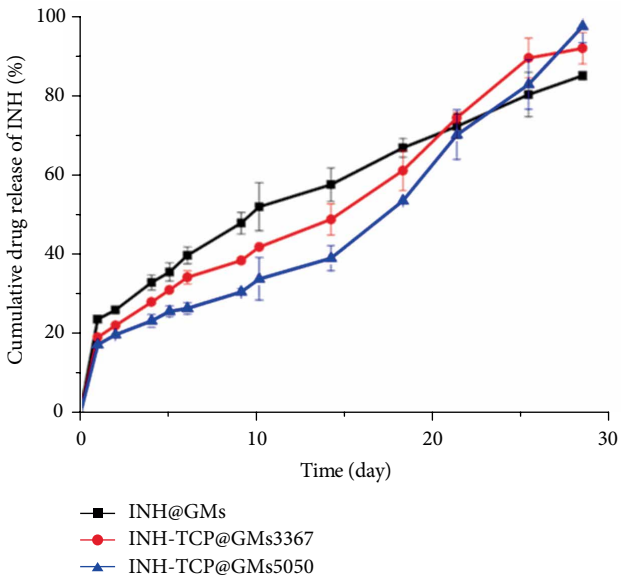

Figure 7: Release behaviours of INH@GMs and INH-TCP@GMs *in vitro*.

The TCP contents of the scaffolds were also in keeping with the theoretical values with the verification by the TGA measurement (Figure 5(a)), indicating the minimal TCP loss during preparation of scaffolds. Since the TCP distribution in scaffolds exerted an influence over bone regeneration, the TCP content of I-M/P50 scaffolds in different parts was also measured by TGA (Figure 5(b)). At the top, middle and bottom parts the content was 21.2 wt%, 24.7 wt% and 27.8 wt%, respectively. The trivial distribution difference of TCP content in the whole scaffolds may be ascribed to a bit of sedimentation of microparticles during the preparing process of scaffolds, but it would not impact the usage of scaffolds.

The *b*-PLGC scaffolds were loaded with INH-TCP@GMs and RFP according to the previous methods [15]. Compared to the I-M/P50, I-M/RP50 was also in possession of random interconnected porous structures in Figure 6. Its pore size was in a range of 200–300 μm along with numerous micro-pores (10–50 μm) on the wall of macro-pores. Besides, the pore porosity and TCP content of the I-M/RP50 scaffolds were also similar to the I-M/P50 scaffolds (the corresponding data and curves were not shown to avoid repetition). These results manifested that the RFP had no obvious influence on the morphology of scaffolds.

3.2. Drug Release Behaviours of b-PLGC Scaffolds Loaded with INH and RFP In Vitro

3.2.1. INH Release Behaviours of Microparticles In Vitro. The initial burst releases of INH@GMs, INH-TCP@GMs3367 and INH-TCP@GMs5050 were 24.4 wt%, 19.8 wt% and 17.9 wt% respectively in Figure 7. As the TCP content was increased, the burst release fell down, indicating that TCP could inhibit the initial burst release to some extent. After the initial burst release, INH release behaviours of these three microparticles were essentially uniform with linear trends. The release rate diminished as the TCP content augmented. But the drug release speed of INH-TCP@GMs accelerated after three weeks of inhibition effect, especially for the INH-TCP@GMs5050 whose cumulative release reached 98.2% on the fourth week, higher than 92.7% in INH-TCP@GMs3367 and 85.7% in INH@GMs.

After 28 days, the morphologies of microparticles were observed Figure 8. Obviously, gelatin microparticles without TCP were still able to maintain their spherical shape while the majority of those particles containing TCP were degraded as well as the exposure of TCP on the surfaces. The higher contents of TCP could cause the quicker degradation for these microparticles, which was consistent with the drug release behaviours after 3 weeks. Based on the above results of high INH entrapment efficiency, slow initial drug release rate and thorough ultimate drug release content, INH-TCP@GMs5050 was an ideal material for fabricating the INH loaded *b*-PLGC scaffolds.

3.2.2. Drug Release Behaviours of INH Loaded b-PLGC Scaffolds In Vitro. Drug release behavior of INH loaded *b*-PLGC scaffolds is shown in Figure 9(a). The initial INH burst release of INH/TCP/*b*-PLGC was higher and the cumulative INH release in the first week exceeded 60%, but that of I-M/P50 and I-M/P70 scaffolds was less than 20%. The sustained INH release of I-M/P50 and I-M/P70 scaffolds could keep for 84 days, and the cumulative release increased with the climbing content of INH-TCP@GMs5050 in scaffolds. The rapid INH

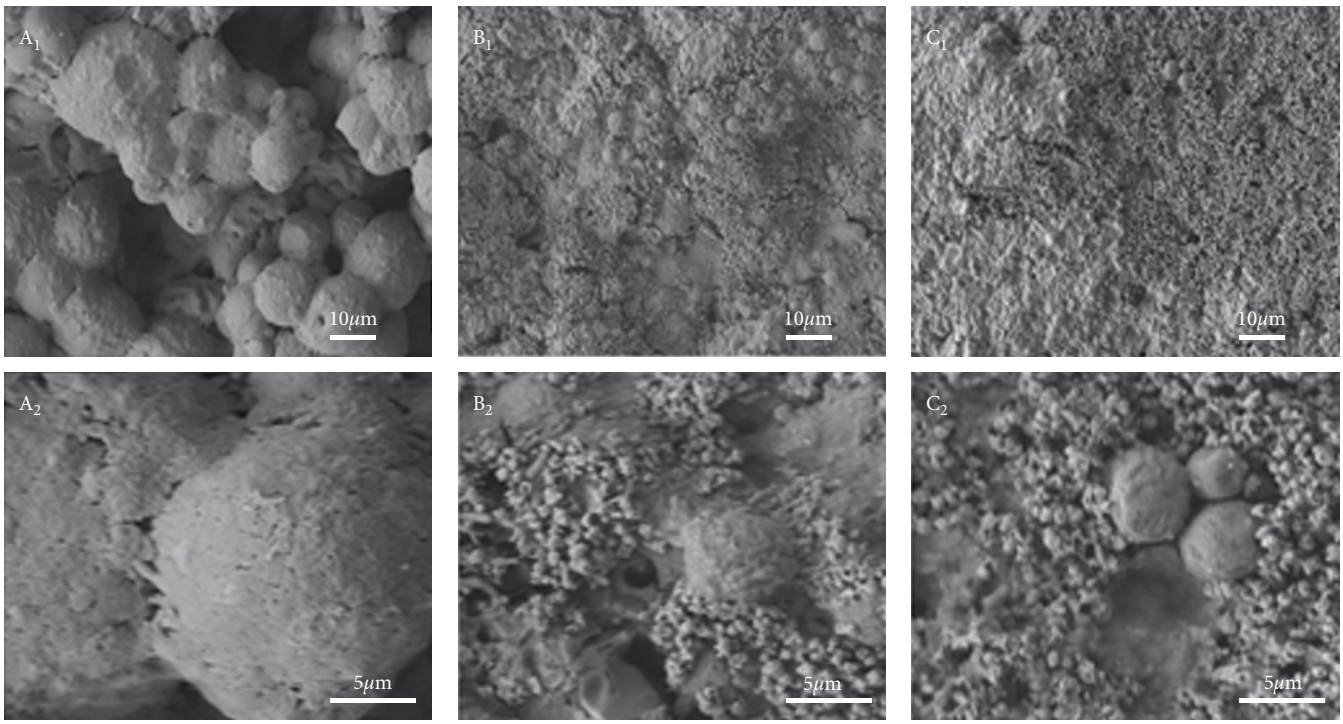

Figure 8: SEM images showing the GMs and TCP@GMs after release for 28 days. (a) GMs; (b) TCP@GMs3367, and (c) TCP@GMs5050.

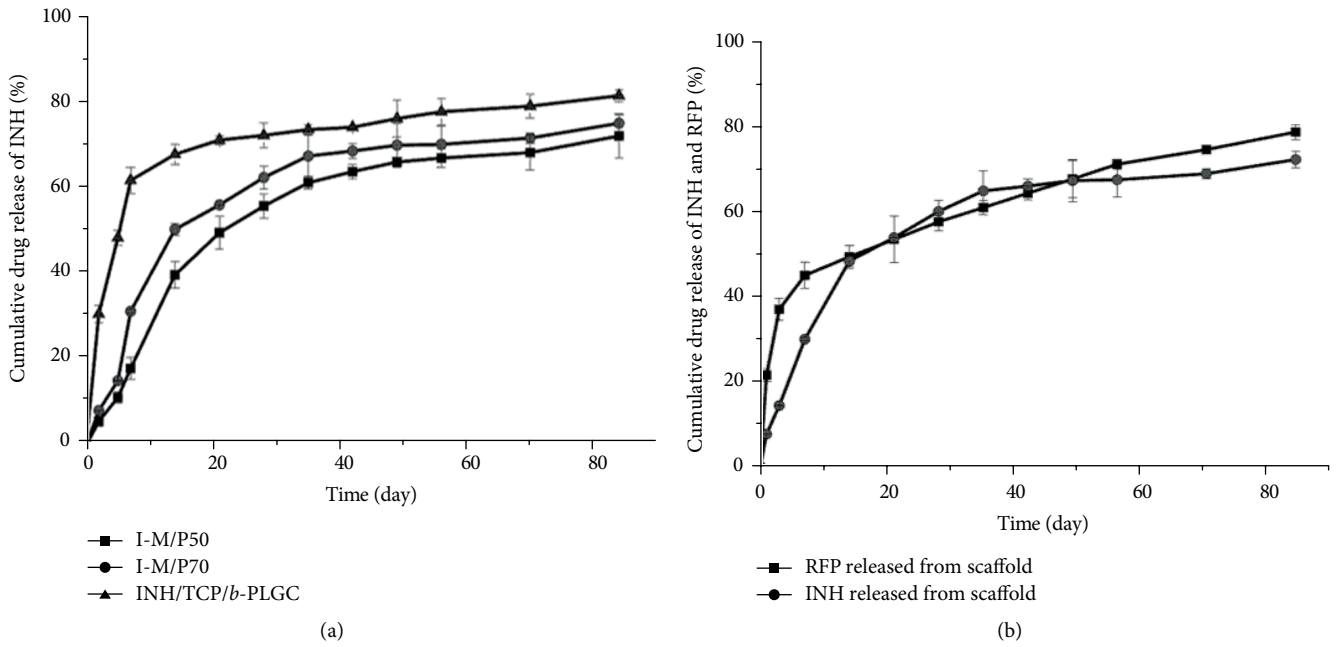

Figure 9: (a) Release behaviours of INH-loaded scaffolds *in vitro*. (b) INH and RFP Release behaviors of I-M/RP50 scaffolds *in vitro*.

release of INH/TCP/*b*-PLGC should be attributed to that of the water-soluble INH was directly blended in the scaffolds that were easy to contact with water. The sustained INH release of *b*-PLGC scaffolds loaded with INH-TCP@GMs5050 was mainly caused by the sustained INH release of INH-TCP@GMs5050. In addition, since microparticles were coated with polymers during scaffold preparation process, some particles were embedded in the inner of scaffolds (Figure 5) and the INH was prevented to be directly in touch with water, resulting in the decreasing initial burst release and prolonging the release time. It is mentioned that this dual drugs-loaded system could achieve the expectant roles of respective drugs without obvious influences with each other.

The INH and RFP release profiles of I-M/RP50 scaffolds were shown in Figure 9(b). At the initial stage, a slight INH and RFP initial burst release occurred with about 15% and 20%, respectively. After that, a long-term sustained INH and RFP release profiles were obtained along with the cumulative release of ca. 75% and 82% on day 84, indicating that I-M/RP50 scaffolds could carry out a sustained INH and RFP

release for 3 months, which resembled the INH and RFP release behavior of individual INH-loaded (Figure 9(b)) and RFP-loaded scaffolds. The initial burst release of RFP should ascribe to inevitably existing RFP molecules on the surface of the substrate during the scaffold preparation. While the RFP molecules embedded inside polymeric matrixes would be slowly released via water molecule interpenetration and RFP diffusion effect. The INH and RFP release *in vivo* and its effect on repair and reconstruction of bone tissue would be further studied in our future work. In addition, there were still inevitably initial outbreak release problems that need to be improved. For example, we will design and fabricate another smart system to achieve the controllable varied-drugs delivery by further combining the supramolecular interactions and covalent bond methods.

4. Conclusions

In summary, we prepared a kind of INH-TCP@GMs microparticles with less initial burst release, higher cumulative release and longer sustained INH release, which was closely related to the TCP contents. After particle leaching combined with phase separation technique for the mixture of INH-TCP@GMs5050 and *b*-PLGC solution containing RFP, INH- and RFP-loaded b-PLGC scaffolds was obtained with the quicker INH release rate than INH-loaded *b*-PLGC scaffolds on account of the evenly distributed microparticles in these scaffolds. This drug release system could achieve their respective roles of two drugs, and the loading process was not affected with each other. After a slight initial burst release occurred on the first day, the INH and RFP were slowly released from the scaffolds for 84 days and the cumulative release achieved about 75% and 82% on day 84, respectively. Thus, we believe that these dual anti-tuberculosis drug-loaded composite scaffolds will have potential clinical applications in bone tuberculosis therapy.

Data Availability

The data used to support the findings of this study are available from the corresponding author upon request.

Conflicts of Interest

The authors declare no conflict of interest.

Authors' Contributions

Dawei Li and Chao Li contributed equally to this work.

Funding

We greatly acknowledge the financial supports from the National Natural Science Foundation of China (NSFC, 81972081 and 21604093), the Beijing Novel Program (Z181100006218059) and the Open Research Project Funds (K2019-27).

References

[1] C. E. Dodd and L. S. Schlesinger, "New concepts in understanding latent tuberculosis," *Current Opinion in Infectious Diseases*, vol. 30, pp. 316–321, 2017.

[2] C. Shi and E. G. Pamer, "Monocyte recruitment during infection and inflammation," *Nature Reviews Immunology*, vol. 11, pp. 762–774, 2011.

[3] Y. R. Wang, Q. J. Wang, R. B. Zhu et al., "Trends of spinal tuberculosis research (1994–2015)," *Medicine*, vol. 95, no. 38, pp. 1994–2015, 2016.

[4] D. J. Short and T. Zgonis, "Management of osteomyelitis and bone loss in the diabetic charcot foot and ankle," *Clinics in Podiatric Medicine and Surgery*, vol. 34, no. 3, pp. 381–387, 2017.

[5] D. Li, L. T. Li, Y. L. Ma et al., "Dopamine-assisted fixation of drug-loaded polymeric multilayers to osteoarticular implants for tuberculosis therapy," *Biomaterials Science*, vol. 5, no. 4, pp. 730–740, 2017.

[6] C. E. Clancy, G. An, W. R. Cannon et al., "Multiscale modeling in the clinic: drug design and development," *Annals of Biomedical Engineering*, vol. 44, pp. 2591–2610, 2016.

[7] Y. J. Gao, Y. S. Ou, Q. X. Deng, B. He, X. Du, and J. Li, "Comparison between titanium mesh and autogenous iliac bone graft to restore vertebral height through posterior approach for the treatment of thoracic and lumbar spinal tuberculosis," *PLoS One*, vol. 12, no. 4, p. e0175567, 2017.

[8] J. Zou, Z. Shi, G. Mei, J. Xue, W. Gu, and X. Li, "Two-stage operation to treat destructive midfoot tuberculosis: 14 cases experience," *Orthopaedics & Traumatology: Surgery & Research*, vol. 102, pp. 1075–1080, 2016.

[9] M. Kalathur, S. Baiguera, and P. Macchiarini, "Translating tissue-engineered tracheal replacement from bench to bedside," *Cellular and Molecular Life Sciences*, vol. 67, no. 24, pp. 4185–4196, 2010.

[10] D. Huang, D. W. Li, T. T. Wang et al., "Isoniazid conjugated poly(lactide-co-glycolide): long-term controlled drug release and tissue regeneration for bone tuberculosis therapy," *Biomaterials*, vol. 52, pp. 417–425, 2015.

[11] M. L. Kang, J. K. Ko, J. E. Kim, and Gun-I. l. Im, "Intra-articular delivery of kartogenin-conjugated chitosan nano/microparticles for cartilage regeneration," *Biomaterials*, vol. 35, pp. 9984–9994, 2014.

[12] R. Garcia-Alvarez, I. Izquierdo-Barba, and M. Vallet-Regi, "3D scaffold with effective multidrug sequential release against bacteria biofilm," *Acta Biomaterialia*, vol. 49, pp. 113–126, 2017.

[13] Y. G. Zhang, Y. J. Zhu, F. Chen, and T. W. Sun, "A novel composite scaffold comprising ultralong hydroxyapatite microtubes and chitosan: preparation and application in drug delivery," *Journal of Materials Chemistry B*, vol. 5, pp. 3898–3906, 2017.

[14] L. H. Nguyen, M. Y. Gao, J. Q. Lin, W. Wu, J. Wang, and S. Y. Chew, "Three-dimensional aligned nanofibers-hydrogel scaffold for controlled non-viral drug/gene delivery to direct axon regeneration in spinal cord injury treatment," *Scientific Reports*, vol. 7, p. 42212, 2017.

[15] P. Zhao, D. W. Li, F. Yang et al., "*In vitro* and *in vivo* drug release behavior and osteogenic potential of a composite scaffold based on poly(ε-caprolactone)-*block*-poly(lactic-*co*-glycolic acid) and β-tricalcium phosphate," *Journal of Materials Chemistry B*, vol. 3, pp. 6885–6896, 2015.

[16] V. Kaushik, J. S. Yakisich, N. Azad et al., "Anti-tumor effects of cardiac glycosides on human lung cancer cells and lung

tumorspheres," *Journal of Cellular Physiology*, vol. 232, pp. 2497–2507, 2017.

[17] S. Suzuki, T. Horinouchi, and C. Furusawa, "Acceleration and suppression of resistance development by antibiotic combinations," *BMC Genomics*, vol. 18, no. 1, 2017.

[18] Y. Zou, Y. Zhang, L. W. Han et al., "Oxidative stress-mediated developmental toxicity induced by isoniazide in zebrafish embryos and larvae," *Journal of Applied Toxicology*, vol. 37, no. 7, pp. 842–852, 2017.

[19] M. Njire, Y. J. Tan, J. Mugweru et al., "Pyrazinamide resistance in mycobacterium tuberculosis: review and update," *Advances in Medical Sciences*, vol. 61, no. 1, pp. 63–71, 2016.

[20] L. M. A. Alvarez, J. M. G. Garcia, M. D. P. Hernandez et al., "Utility of phenotypic and genotypic testing in the study of mycobacterium tuberculosis resistance to first-line anti-tuberculosis drugs," *Archivos de Bronconeumología*, vol. 53, pp. 192–198, 2017.

[21] M. J. Chang, B. Jin, J. W. Chae et al., "Population pharmacokinetics of moxifloxacin, cycloserine, p-aminosalicylic acid and kanamycin for the treatment of multi-drug-resistant tuberculosis," *International Journal of Antimicrobial Agents*, vol. 49, no. 6, pp. 677–687, 2017.

[22] L. F. Diniz, P. S. Carvalho, C. C. de Melo, and J. Ellena, "Development of a salt drug with improved solubility: ethionamide nitrate," *Journal of Molecular Structure*, vol. 1137, pp. 119–125, 2017.

[23] T. Maimakov, L. Sadykova, Z. Kalmataeva, K. Kurakpaev, and K. Šmigelskas, "Treatment of tuberculosis in south kazakhstan: clinical and economical aspects," *Medicina*, vol. 49, pp. 335–340, 2013.

[24] H. Shen, X. X. Hu, F. Yang, J. Bei, and S. Wang, "Cell affinity for bFGF immobilized heparin-containing poly(lactide-co-glycolide) scaffolds," *Biomaterials*, vol. 32, pp. 3404–3412, 2011.

[25] F. Yang, W. J. Cui, Z. Xiong, L. Liu, and J. S. Bei Wang, "Poly(L, L-lactide-co-glycolide)/tricalcium phosphate composite scaffold and its various changes during degradation in vitro," *Polymer Degradation and Stability*, vol. 91, pp. 3065–3073, 2006.

[26] S. Khan, M. Ul-Islam, M. Ikram et al., "Three-dimensionally microporous and highly biocompatible bacterial cellulose-gelatin composite scaffolds for tissue engineering applications," *RSC Advances*, vol. 6, pp. 110840–110849, 2016.

[27] H. Shen, Y. Niu, X. Hu, F. Yang, S. Wang, and D. Wu, "A biomimetic 3D microtubule-orientated poly(lactide-*co*-glycolide) scaffold with interconnected pores for tissue engineering," *Journal of Materials Chemistry B*, vol. 3, pp. 4417–4425, 2015.

[28] H. Shen, X. Hu, H. Cui et al., "Fabrication and effect on regulating vSMC phenotype of a biomimetic tunica media scaffold," *Journal of Materials Chemistry B*, vol. 4, pp. 7689–7696, 2016.

[29] A. Galperin, J. L. Thomas, and D. R. Buddy, "Degradable, thermo-sensitive poly(N-isopropyl acrylamide)-based scaffolds with controlled porosity for tissue engineering applications," *Biomacromolecules*, vol. 11, no. 10, pp. 2583–2592, 2010.

[30] W. Teng, T. J. Long, Q. Zhang, K. Yao, T. T. Shen, and B. D. Ratner, "A tough, precision-porous hydrogel scaffold: ophthalmologic applications," *Biomaterials*, vol. 35, no. 32, pp. 8916–8926, 2014.

[31] H. K. Makadia and S. J. Siegel, "Polylactic-co-glycolic acid (PLGA) as biodegradable controlled drug delivery carrier," *Polymers*, vol. 3, pp. 1377–1397, 2011.

[32] F. J. O'Brien, B. A. Harley, I. V. Yannas, and L. J. Gibson, "The effect of pore size on cell adhesion in collagen-GAG scaffolds," *Biomaterials*, vol. 26, pp. 433–441, 2005.

Hindawi
Advances in Polymer Technology
Volume 2019, Article ID 9536320, 8 pages
https://doi.org/10.1155/2019/9536320

Research Article

Fabricated of Superhydrophobic Silanized Melamine Sponge with Photochromic Properties for Efficiency Oil/Water Separation

Peng Hong,[1,2] **Zhu Liu**,[1] **Yang Gao**,[1] **Yubin Chen**,[1] **Mingxun Zhuang**,[1] **Lijuan Chen**,[1] **Xiaoxuan Liu**,[1] **and Hongping Xiang**[1]

[1]*Guangdong Provincial Key Laboratory of Functional Soft Condensed Matter, School of Materials and Energy, Guangdong University of Technology, Guangzhou 510006, Guangdong, China*
[2]*Zhongshan Forensic Science Institute, Zhongshan 528400, Guangdong, China*

Correspondence should be addressed to Xiaoxuan Liu; p-xxliu@gdut.edu.cn and Hongping Xiang; xianghongping@gdut.edu.cn

Received 20 June 2019; Accepted 26 August 2019; Published 13 November 2019

Guest Editor: Xiaosong Cao

Superhydrophobic sponge as potential absorbing material for oil/water separation is attracting great attention recently. However, there are still some challenges to feasibly fabricate superhydrophobic sponge with large scale and low cost. Herein, a novel photochromic superhydrophobic melamine sponge (PDMS-SP sponge) is fabricated by facilely dip-coating and thermocuring of hydroxyl-terminated polydimethylsiloxanes mixed with photochromic spiropyran. FT-IR, EDS, and XPS results confirm the successful coating of PDMS-SP upon melamine sponge. The resultant sponge not only possesses excellent water repellency with a contact angle of 154.5° and oil-water separation efficiency with an oil absorption capacity of 48–116 folds of itself weight, but also shows photochromic phenomenon between colorless and purple when it is successively exposed to UV irradiation and visible light.

1. Introduction

Along with the rapid development of urbanization and industrialization, water pollution from oil pollutants and oil leakage is increasingly severe that has caused serious damages to human health and ecological balance. For example, about 4.9 million barrels of oil spill in the Gulf of Mexico in 2010 and cover thousands of square kilometers of sea, which cause a great harm to local marine and aquatic ecosystems [1–5]. Therefore, the effective separation of oil from water is a major concern. Traditional oil separation techniques can be summarized as physical, chemical, and biological methods, such as *in-situ* burning, dispersants, activated carbon [6], cotton fiber [7] exploited for spilled oil. Nevertheless, traditional separation materials have high cost, poor selectivity, and nonrecyclability. Fortunately, the rapid development of interface science provides a more efficient solution to separate oil from mixtures [8].

Superhydrophobic interfaces, including two-dimensional materials [9–15] and three-dimensional porous materials [16–23], can realize effective oil and water separation. The two-dimensional meshes or membranes need to be treated before oil water separation, but the three-dimensional superhydrophobic porous materials are promising solution with low energy. Various advanced 3D porous materials, such as foam, sponge, aerogel, and xerogel materials have been developed and show high selectivity and outstanding absorption capacity toward various oils and organic solvents [24–27]. Pham and Dickerson [28] explore a robust superhydrophobic 3D porous materials by the silanization of commercial melamine (MA) sponge, which reveals a water contact angle of 151.0°, good adsorption ability to a variety of organic solvents and grease, and excellent recyclability. Especially, the polysiloxane backbone exhibits a low surface tension value of around 21 mN/m that is suitable for water repellency [29]. Peng et al. [30] introduce a facile dip-coating/UV-curing method to prepare superhydrophobic and oleophilic melamine sponge, coated polydimethylsiloxane (PDMS) film onto the sponge skeleton through UV-assisted thio–ene click reactions. Dip-coating offers a robust and effective approach in large-scale preparation of a superhydrophobic sponge, which exhibits an absorption capacity of 103–179 folds its own weight. Therefore, silanized sponge is an efficient and economical method to explore three-dimensional oil-water separation materials.

In recent years, some advanced materials can respond to external stimuli (e.g., light, magnetic, thermal, and pH) and are employed in oil/water separation [31–36]. Light energy,

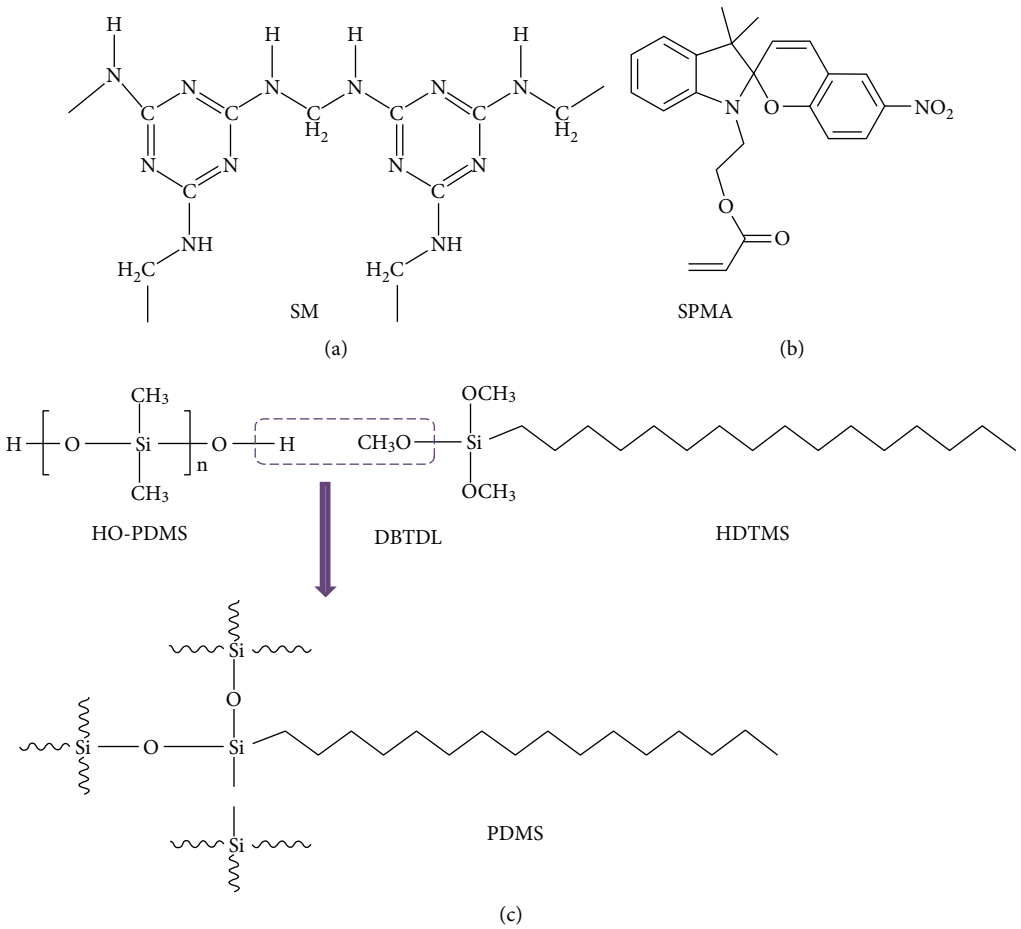

Figure 1: (a) Chemical structure of pristine melamine sponge, (b) chemical structure of SPMA, (c) schematic rout of PDMS thermocuring.

due to clean and convenient, has drawn more and more attention. Spiropyran (SP) is a photosensitive molecule featuring reversible optical-switching between two forms, the colorless ring-closed SP form and the colored ring-opened merocyanine (MC) form [37]. In our group, epoxy resin is thoroughly mixed with an SP derivative to formulate anti-counterfeiting coatings that could be applied to flexible substrates, such as food and medicine packaging [38]. Spiropyran (SP)-containing fluorinated polyacrylate (F-PA-SP) latex is prepared by emulsion polymerization, which is potential to cellulosic paper with outstanding reversible color changes and hydrophobicity [39].

Herein, a novel photochromic superhydrophobic sponge is developed by dip-coating and thermocuring of commercial melamine-formaldehyde (SM) sponge with polydimethylsiloxane (PDMS) mixtures containing spiropyran methacrylate (SPMA) as photochromic motif, and hexadecyltrimethoxysilane as multi cross-linker. After thermocuring, PDMS is covalently covered on the surface of the sponge, and SPMA is restricted in the cured rubber. Compared to other chemical methods of grafting SP to SM, this is a new simple physical way to cover SPMA on the surface of a sponge. By simple UV irradiation, PDMS-SP-coated melamine sponge transforms from colorless to purple. Next, the superhydrophobicity for oil/water separation and photochromic behavior of (PDMS)-coated melamine sponge are studied. In addition, the internal porosity, thermal, and chemical stability of SM endows PDMS-SP-coated melamine sponge with high absorption capacity (116 times) for oil absorption. These findings also exhibit potential applications to indicate the depth of UV curing three-dimensional porous materials.

2. Materials and Methods

2.1. Materials. Melamine sponge was purchased from a commercial store (7.90×10^{-3} g/cm^3). The hydroxyl-terminated polydimethylsiloxane (HO-PDMS) with a viscosity of 5000 MPa·s was provided by Gangzhou Juchen Zhaoye Organic Silicone Co., Ltd. Hexadecyltrimethoxysilane (HDTMS), dibutyltin dilaurate (DBTDL) and cetane were purchased from Aladdin Reagent Co., Ltd. (Shanghai, China). All chemicals used as received without further purification. 1′-(2-Methacryloxyethyl)-3′,3′-dimethyl-6-nitro-spiro(2H-1-benzopyran-2′,2′-indoline) (SPMA) was synthesized according to previous work [39], showed in Figure 1(b).

2.2. Preparation of Superhydrophobic PDMS-SP Melamine Sponge. The dip-coating and thermocuring process were implemented according to the reported method [30] with modification, showed in Figure 1(c). The HO-PDMS 2.5 g,

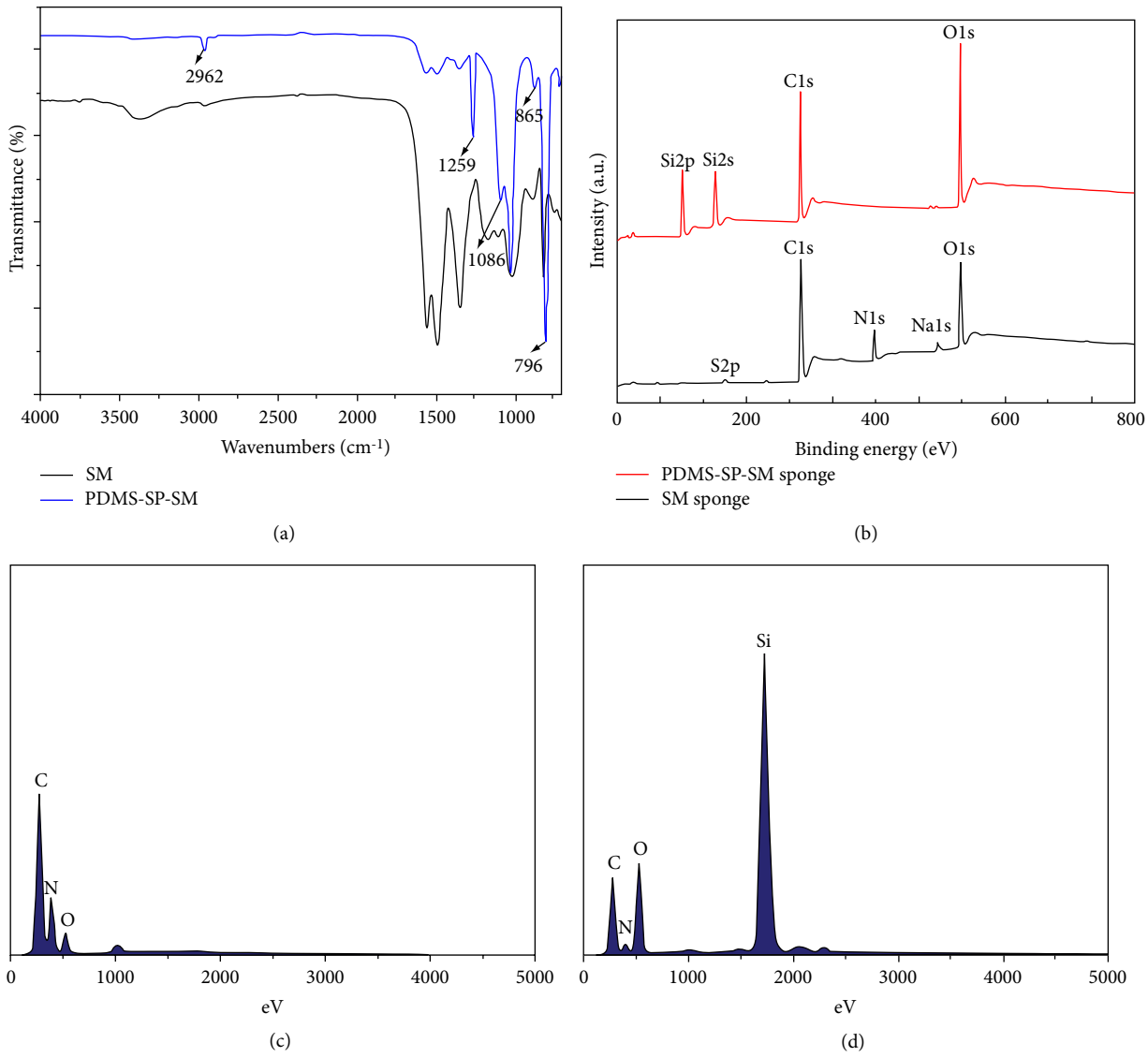

FIGURE 2: (a) ATR-FTIR spectra of pristine melamine sponge and PDMS-SP modified melamine sponge, (b) XPS spectra of pristine melamine sponge and PDMS-SP modified melamine sponge, (c) EDS spectra of pristine melamine sponge on the sponge framework surface, (d) EDS spectra of PDMS-SP modified melamine sponge.

HDTMS 0.25 g, SPMA 0.008 g, and DBTDL 0.05 g were dissolved in 25 mL CH_2Cl_2. The pristine melamine sponge was cut into $1 \times 1 \times 1\ cm^3$ pieces and were immersed in the above mixture for 5 min. Then removed from the solution and squeezed to extract the absorbed solution, cured at 50°C for 10 min. It was then repeatedly washed with CH_2Cl_2 using the sorption/squeezing process for the removal of any untreated starting materials. Finally, it was dried in air for 6 h, The PDMS-SP-coated melamine sponge obtained.

2.3. Oil Absorption Experiments. The absorption capacities of PDMS-SP-coated sponge for various oils and organic solvents were determined by dipping a piece of PDMS-SP-coated sponge into the liquid (oil or organic solvent) until the sponge was saturated with the liquid and left to drip for 30 s for weighting. Repeated sorption/squeezing processes were used to evaluate recyclability of PDMS-SP-coated sponge.

2.4. Characterization. Attenuated total reflection-Fourier transform infrared (ATR-FTIR) spectra were collected 4000 and 500 cm^{-1} on a Nicolet iS50 spectrometer with a 4 cm^{-1} resolution over 32 scans. The micromorphology was observed by SEM on an SU-8010 (Hitachi Ltd., Japan) field emission electron microscope at an accelerating voltage of 5 kV. Samples were coated with a thin gold layer before SEM analysis. An energy-dispersive X-ray spectrometer fitted to the scanning electron microscope was used for chemical elemental identification. The wetting properties of PDMS-coated sponge were investigated by static contact angle measurements at room temperature using an OCA 15Pro contact angle goniometer with a droplet volume of 5 μL and each contact angle was average of 5 different positions for each sample. X-ray photoelectron spectroscopy (XPS) measurement was performed on a Kratos ESCA spectrometer (Axis Ultra DLD) with an Al Kα X source (150 W, 15 kV) at a take-off angle of 45° from the normal surface.

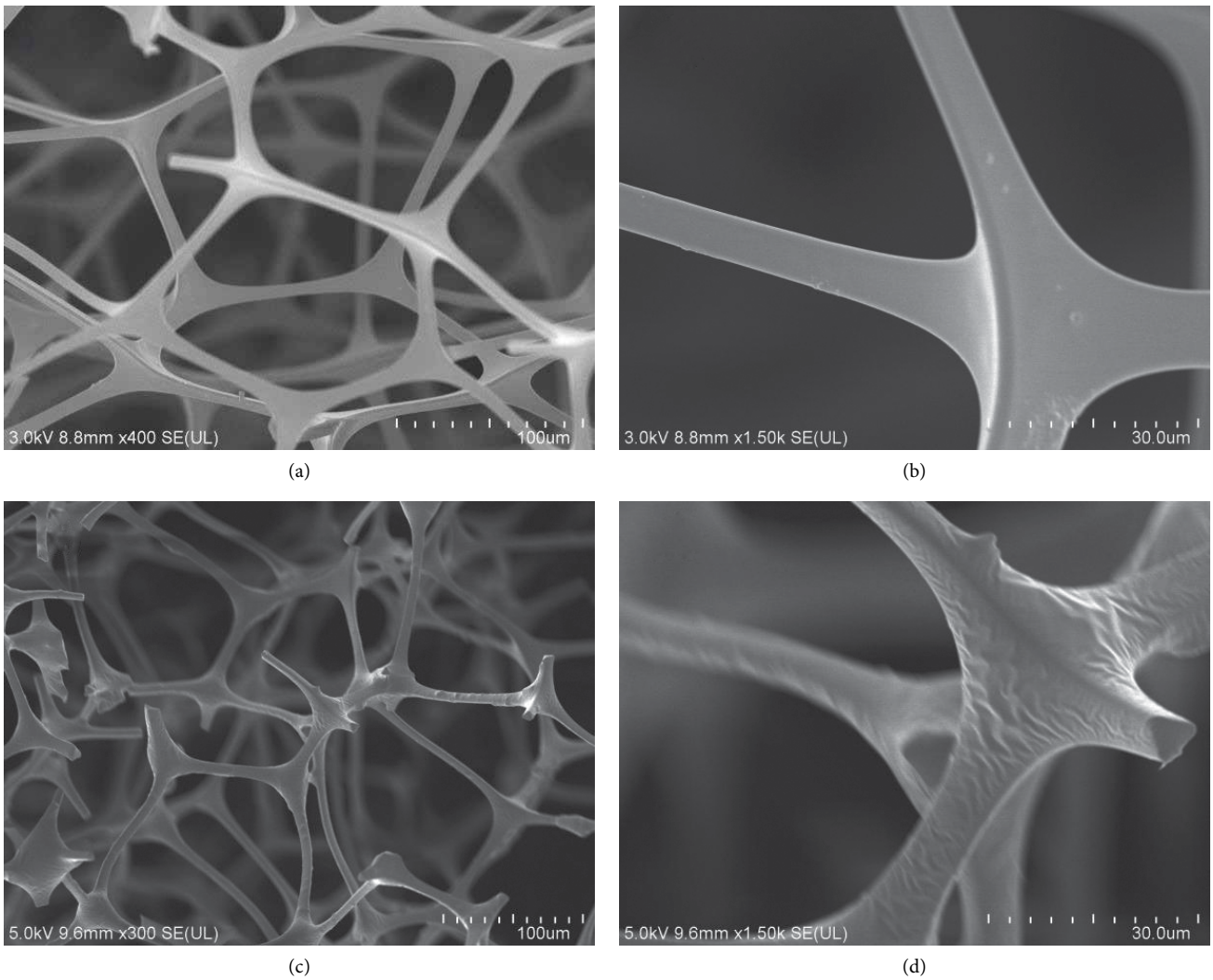

Figure 3: (a, b) SEM images of a pristine melamine sponge and (c, d) PDMS-SP modified melamine sponge.

3. Results and Discussion

3.1. Characterizations of PDMS-SP Melamine Sponge. Figure 2(a) shows the ATR-FTIR spectra of untreated SM melamine sponge and PDMS-SP-coated melamine sponge. The spectrum of SM displayed prominent peaks at 811, 1163, 1546, and 3383 cm^{-1} that are assigned to triazine ring bending, C–O stretching, C=N stretching, and N–H (of the secondary amine) stretching, respectively. Peaks centered at 1343 cm^{-1} and 1483 cm^{-1} are indicative of C–H bending. After dip-coating with PDMS, the spectrum of PDMS-SP-coated melamine sponge show obviously absorption band near 1259 cm^{-1} is attributed to symmetric deformation of the $-CH_3$ group in $-Si(CH_3)_2$ of HO-PDMS, and the bands located at 865 $cm^{-1}$and 796 $cm^{-1}$are assigned to Si–C and Si–O vibration, 2962 cm^{-1} and 1086 cm^{-1} are ascribed to stretching vibrations of $-CH_3$, and Si–O–Si groups in the HO-PDMS [40] respectively.

Figure 2(b) shows the XPS curves of untreated melamine sponge and PDMS-SP modified melamine sponge. The spectrum in Figure 1(b) SM sponge indicates five elements, including C, N, O, S, and Na which is consistent with the composition of commercial sponge [28]. Both samples exhibit a C1s peak at 284.8 eV and an O1s peak at 532.3 eV. Moreover, Si2s and Si2p peaks were found at 165.6 eV and 102.4 eV, respectively. This indicates that PDMS-SP was successfully coated to sponge frame by dipping-coating. The N1s peak located at 398.3 eV was detected on pristine melamine surface and disappeared in PDMS-SP-modified sponge spectrum. This is because that the small amount of nitrogen species is completely covered by PDMS-SP layer. As shown in Figure 2(c), three elements C, N, and O are detected by EDS in pristine melamine sponge. As expected, silicon in PDMS-SP modified melamine sponge is shown in EDS spectrum of Figure 2(d). Togethering with XPS results, it demonstrates the coating of silicone chains on melamine sponge surface.

The morphologies of melamine sponge before and after PDMS-SP-coating are examined by SEM and shown in Figure 3. The melamine sponge comprises a three-dimensional, elasticity, porous structure with pore sizes in the range of 100–150 μm (Figure 3(a)). The skeletons of the melamine sponge are smooth with an average diameter of ~10 μm (Figure 3(b)). Compared to the pristine melamine sponge, PDMS-SP-coated melamine sponge have significant changed morphologies. The porous structure of sponge is not destroyed

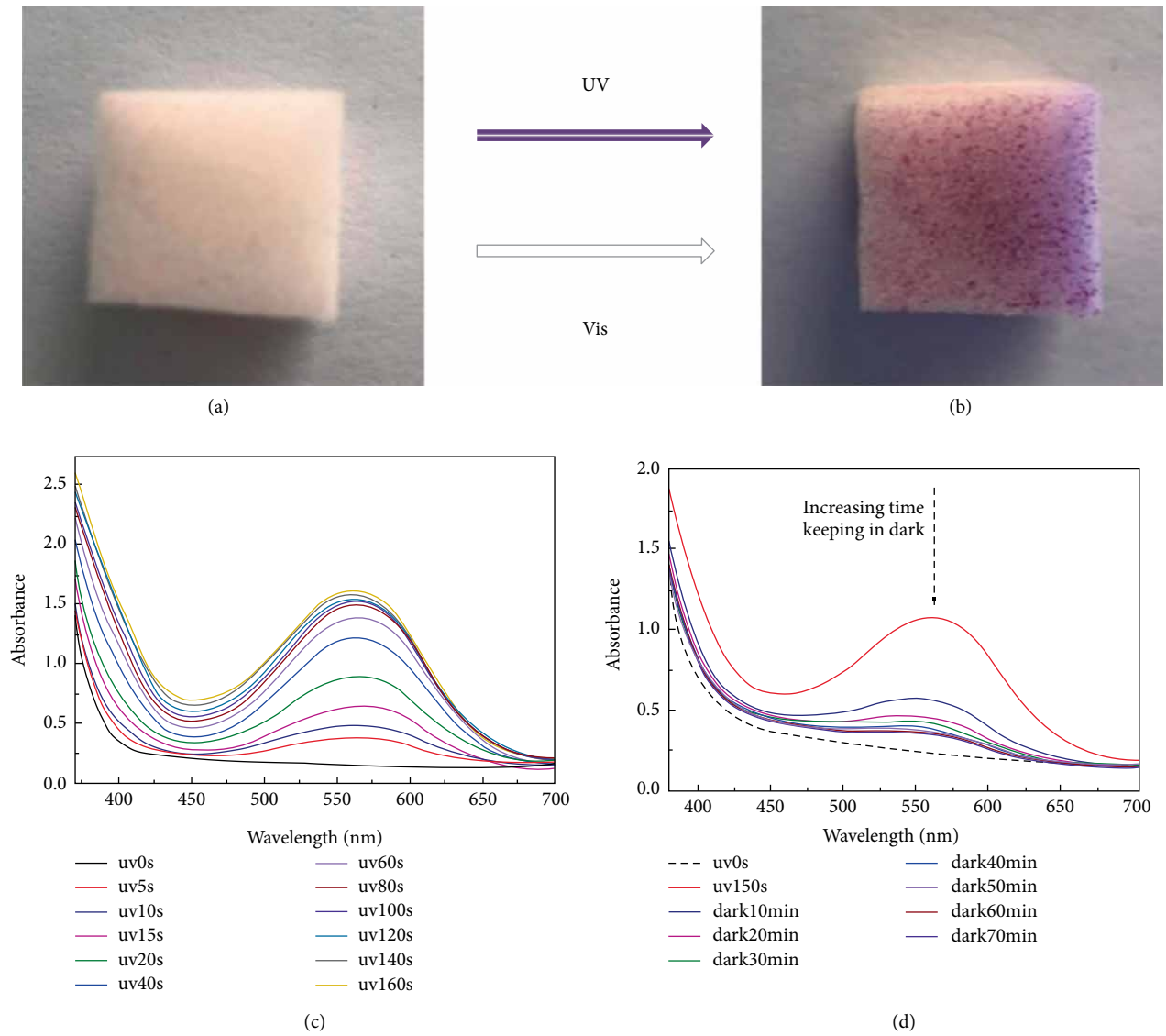

FIGURE 4: (a, b) Photochromic coloration of PDMS-SP modified melamine sponge under UV irradiation, (c) absorbance curves of cross-linked PDMS/SPMA after UV irradiation, (d) absorbance changes with exposure time under UV/vis irradiation.

during the dipping-coating process. However, it is obviously observed that the 3D skeleton of sponge became rough after dipping-coating and regularly arranged resembling strips are observed throughout the whole sponge skeleton (Figures 3(c) and 3(d)). Curing-induced shrinkage and migration of silicone result in undulating wrinkles with an average distance between these strips less than 3 μm, and the width of these strips is about 1 μm. These results indicate that PDMS-SP solution can be adhered to the surface of sponge skeleton fibers uniformly by thermocuring.

3.2. PDMS-SP Melamine Sponge with Photochromic Properties. As reported, spiropyran is a photosensitive molecule featuring reversible optical-switching between two forms [30]. As shown in Figures 4(a) and 4(b), PDMS-SP-coated melamine sponge transforms from colorless to purple upon exposure to UV irradiation ($\lambda = 365$ nm), while it can reversibly change from purple to colorless as irradiated with visible light. Before UV irradiation, no obvious absorbance of PDMS-SP sample in the range of 450–700 nm. Figure 4(c) illustrates the absorbance curves of the samples upon exposure to UV irradiation for 0 and 160 s. A distinct absorption peak appears at 555 nm due to the transformation of SP into MC form, the observed absorption intensity increases markedly with exposure time. When the purple sample is immediately irradiated with a fluorescent lamp, the absorption peak at 555 nm clearly decreases with the irradiation time and the latex color fades (Figure 4(d)).

3.3. Superwetting and Oil/water Separation of Sponge. The pristine melamine sponge exhibits amphiphilic properties with water contact angles (WCA) and an oil contact angles (OCA) of hexadecane closed to 0°, while PDMS-SP coated sponge was hydrophobic and oleophilic (Figure 5). The difference in PDMS-SP coated sponge is reflected in its wetting property as

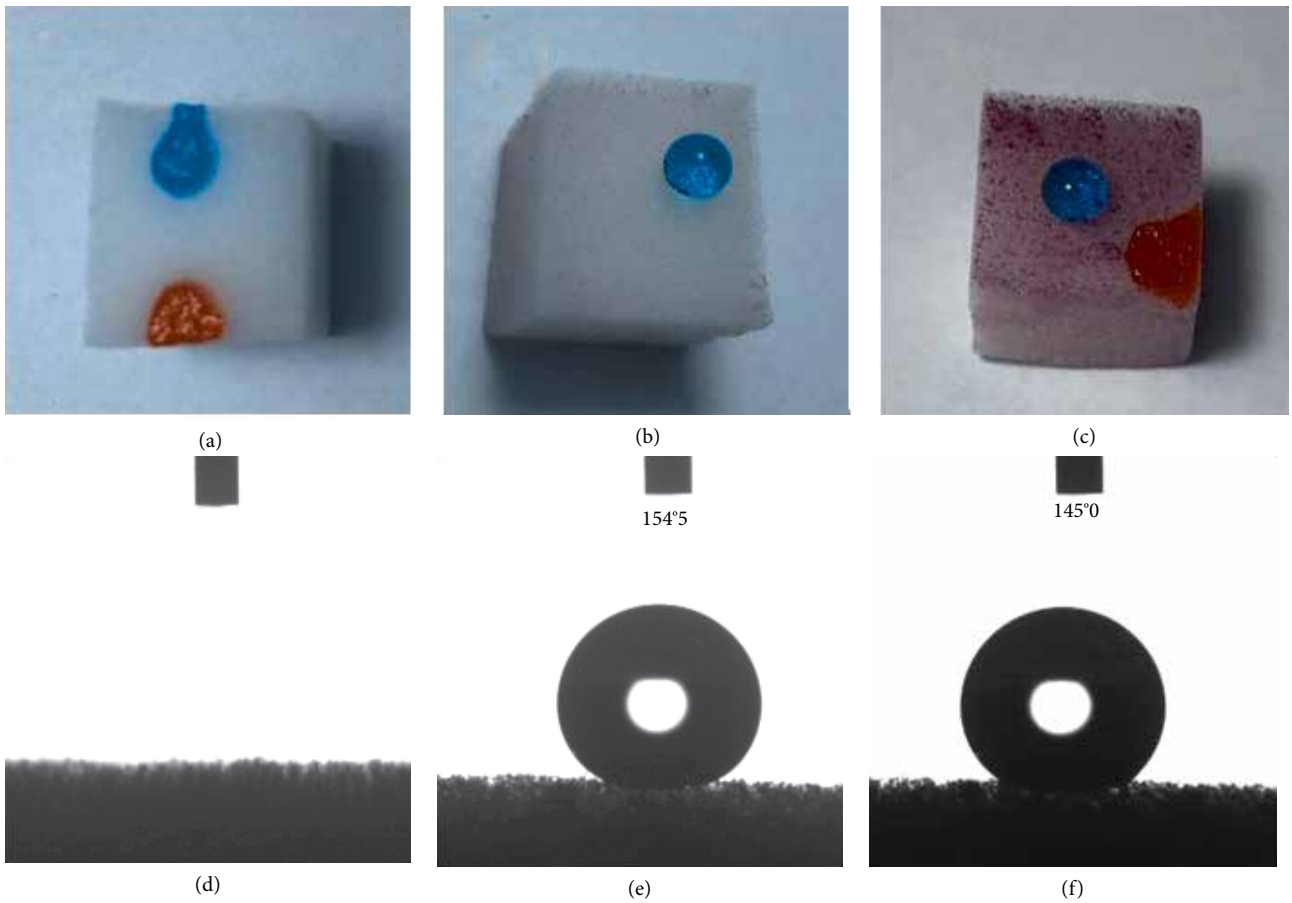

Figure 5: Superwetting of PDMS-coated sponge. (a) Amphiphilic property of pristine melamine sponge. (b) Superhydrophobic of PDMS-SP coated melamine sponge. (c) Hydrophobic and oleophilic property of PDMS-SP coated melamine sponge after UV irradiation. Contact angles of (d) pristine melamine sponge, (e) PDMS-SP coated melamine sponge, and (f) PDMS-SP coated melamine sponge after UV irradiation.

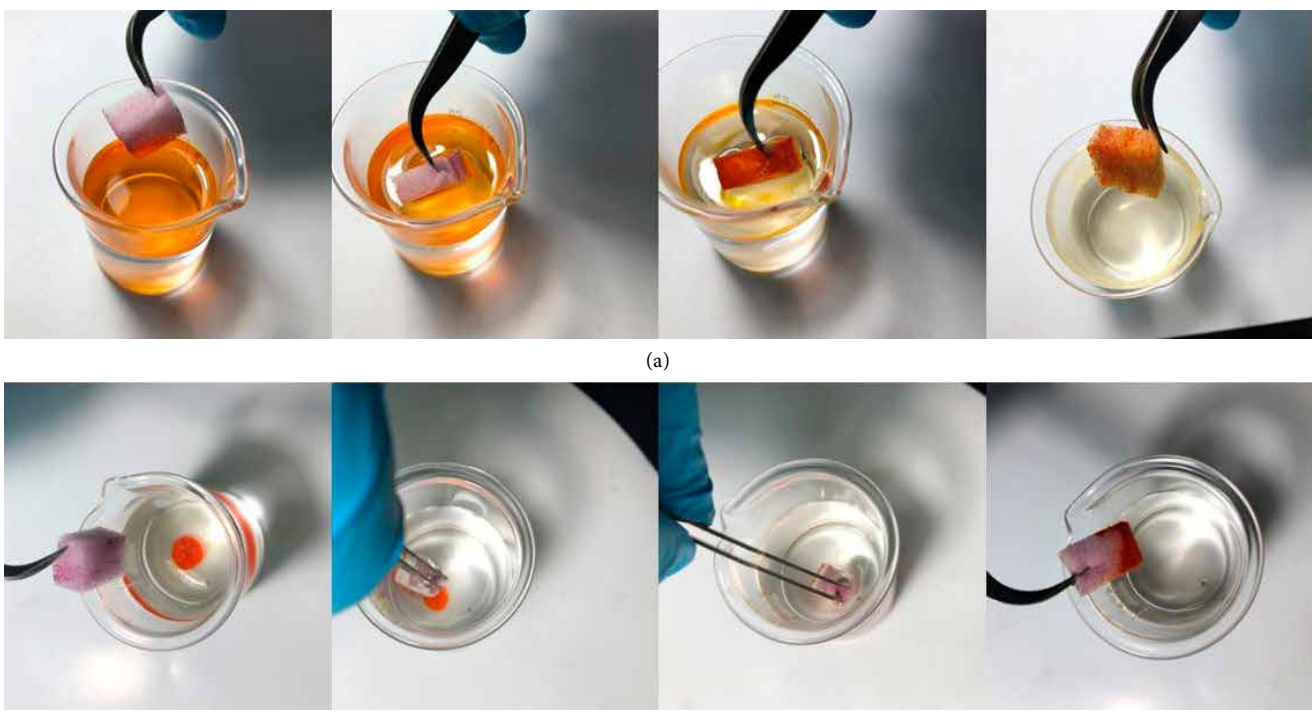

Figure 6: Photographs of the selective sorption of oil with the PDMS-SP coated melamine sponge. The oil was dyed with Sudan I. (a) Hexadecane as oil. (b) Chloroform as oil.

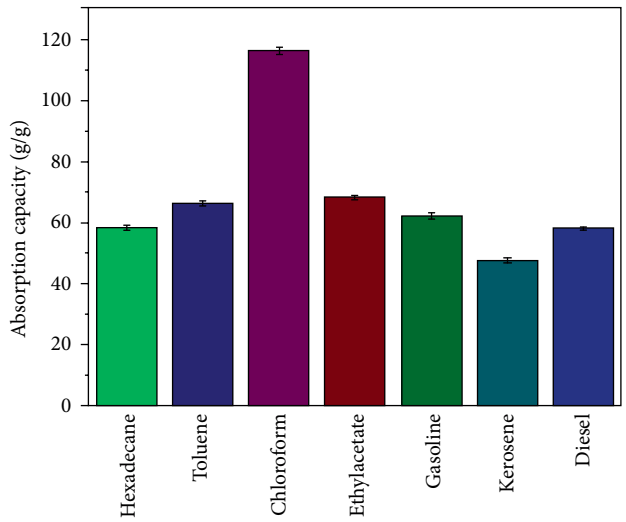

Figure 7: Absorption capacities of the PDMS-SP sponge for different organic solvents and oils.

contacted with water. To further demonstrate the wettability of the raw sponge, water contact angle (CA) is performed by placing droplet of deionized water on PDMS-SP surface. As shown in Figure 5(e), the WCA of PDMS-SP sponge notably increased from 0° for the raw SM sponge to 154.5 ± 1.1°. After UV irradiation, not only the color of sponge changed, but also WCA has a small amount of reducing to 145.0 ± 1.8° showed in Figure 5(f), OCA was still about 0°.

The superhydrophobic surface and porous structure make PDMS-SP coated melamine sponge a viable material for the rapid removal of various organic solvents and oils from water. Selective sorption is a crucial property of oil/water separation materials. The high selective sorption capability of PDMS-SP sponge is showed in Figure 6, both oil float hexadecane (dyed with Sudan I) and sank chloroform (dyed with Sudan I) are removed quickly and completely when the purple color PDMS-SP coated melamine sponge was in contact with oils, then store it in the porous of sponge. The PDMS-SP coated melamine sponge has different sorption performances with different oils and organic solvents. In this test, some common pollutants in industry, such as gasoline, diesel, and toluene etc., are collected.

Figure 7 shows the maximum sorption capacity for oils and solvents in oil/water mixtures, it exhibits excellent absorption capacity in the range 48–116 times of itself weight. The excellent oil/solvent separation capacity is attributed to the highly porous structure as well as the oleophilic properties. In addition to oil absorption, PDMS-SP coated sponge also has photochromic properties. It is well-known that UV curing of three-dimensional porous structure materials is a confusing problem, and the chromic properties can provide intuitive tracking and visualized proof for the research of curing depth.

4. Conclusions

In summary, a superhydrophobic PDMS-SP coated melamine sponge is fabricated with a facile method of dip-coating and thermocuring. The developed PDMS-SP sponge not only absorbs various oil in oil/water mixture with high absorption capacity and selectively, but also changes its color from colorless to purple upon exposure to UV irradiation. These results suggest that the superhydrophobic PDMS-SP sponge may not only provide great potential application for oil recovery, but it also shows potential applications in construction of UV curing three-dimensional porous materials.

Data Availability

The data used to support the findings of this study are available from the corresponding author upon request.

Conflicts of Interest

The authors declare that they have no conflicts of interest.

Acknowledgments

The authors thank the support from the National Natural Science Foundation of China (Grants 51873043 and 21604014), Zhongshan Public Welfare Foundation (Grant 2018B1111).

References

[1] R. K. Gupta, G. J. Dunderdale, M. W. England, and A. Hozumi, "Oil/water separation techniques: a review of recent progresses and future directions," *Journal of Materials Chemistry A*, vol. 5, no. 31, pp. 16025–16058, 2017.

[2] R. Camilli, C. M. Reddy, D. R. Yoerger et al., "Tracking hydrocarbon plume transport and biodegradation at deepwater horizon," *Science*, vol. 330, no. 6001, pp. 201–204, 2010.

[3] E. B. Kujawinski, M. C. Kido Soule, D. L. Valentine, A. K. Boysen, K. Longnecker, and M. C. Redmond, "Fate of dispersants associated with the deepwater horizon oil spill," *Environmental Science & Technology*, vol. 45, no. 4, pp. 1298–1306, 2011.

[4] M. Ge, C. Cao, J. Huang et al., "Rational design of materials interface at nanoscale towards intelligent oil–water separation," *Nanoscale Horizons*, vol. 3, no. 3, pp. 235–260, 2018.

[5] S. Das, S. Kumar, S. K. Samal, S. Mohanty, and S. K. Nayak, "A review on superhydrophobic polymer nanocoatings: recent development and applications," *Industrial & Engineering Chemistry Research*, vol. 57, no. 8, pp. 2727–2745, 2018.

[6] M. Lillo-Ródenas, D. Cazorla-Amorós, and A. Linares-Solano, "Behaviour of activated carbons with different pore size distributions and surface oxygen groups for benzene and toluene adsorption at low concentrations," *Carbon*, vol. 43, no. 8, pp. 1758–1767, 2005.

[7] G. Deschamps, H. Caruel, M.-E. Borredon, C. Bonnin, and C. Vignoles, "Oil removal from water by selective sorption on hydrophobic cotton fibers. 1. Study of sorption properties and comparison with other cotton fiber-based sorbents," *Environmental Science & Technology*, vol. 37, no. 5, pp. 1013–1015, 2005.

[8] L. Feng, Z. Zhang, Z. Mai et al., "A super-hydrophobic and super-oleopshilic coating mesh film for the separation of oil and water," *Angewandte Chemie International Edition*, vol. 43, no. 15, pp. 2012–2014, 2004.

[9] Q. Chen, D. Leon, and R. C. Advincula, "Inorganic-organic thiol-ene coated mesh for oil/water separation," *ACS Applied Materials & Interfaces*, vol. 7, no. 13, pp. 18566–18573, 2015.

[10] S. Qiang, K. Chen, Y. Yin, and C. Wang, "Robust UV-cured superhydrophobic cotton fabric surfaces with self-healing ability," *Materials & Design*, vol. 116, pp. 395–402, 2017.

[11] L. Xiong, W. Guo, B. M. Alameda, R. K. Sloan, W. D. Walker, and D. L. Patton, "Rational design of superhydrophilic/superoleophobic surfaces for oil–water separation via thiol–acrylate photopolymerization," *ACS Omega*, vol. 3, no. 8, pp. 10278–10285, 2018.

[12] P. Varshney, D. Nanda, M. Satapathy, S. Mohapatra, and A. Kumar, "A facile modification of steel mesh for oil/water separation," *New Journal of Chemistry*, vol. 41, pp. 7463–7471, 2017.

[13] Z. Du, P. Ding, X. Tai, Z. Pan, and H. Yang, "Facile preparation of Ag-coated superhydrophobic/superoleophilic mesh for efficient oil/water separation with excellent corrosion resistance," *Langmuir*, vol. 34, no. 23, pp. 6922–6929, 2018.

[14] X. Zeng, S. Xu, P. Pi et al., "Polymer-infiltrated approach to produce robust and easy repairable superhydrophobic mesh for high-efficiency oil/water separation," *Journal of Materials Science*, vol. 53, no. 14, pp. 10554–10568, 2018.

[15] F. Li, Z. Wang, S. Huang, Y. Pan, and X. Zhao, "Flexible, durable, and unconditioned superoleophobic/superhydrophilic surfaces for controllable transport and oil–water separation," *Advanced Functional Materials*, vol. 28, no. 20, p. 1706867, 2018.

[16] Q. Zhu, Y. Chu, Z. Wang et al., "Robust superhydrophobic polyurethane sponge as a highly reusable oil-absorption material," *Journal of Materials Chemistry A*, vol. 1, no. 17, pp. 5386–5393, 2013.

[17] Z. Xiao, M. Zhang, W. Fan et al., "Highly efficient oil/water separation and trace organic contaminants removal based on superhydrophobic conjugated microporous polymer coated devices devices," *Chemical Engineering Journal*, vol. 326, pp. 640–646, 2017.

[18] J. Wang, H. Wang, and G. Geng, "Highly efficient oil-in-water emulsion and oil layer/water mixture separation based on durably superhydrophobic sponge prepared via a facile route," *Marine Pollution Bulletin*, vol. 127, pp. 108–116, 2018.

[19] J. Chen, H. You, L. Xu, T. Li, X. Jiang, and C. M. Li, "Facile synthesis of a two-tier hierarchical structured superhydrophobic-superoleophilic melamine sponge for rapid and efficient oil/water separation," *Journal of Colloid & Interface Science*, vol. 506, pp. 659–668, 2017.

[20] P. Saha and L. Dashairya, "Reduced graphene oxide modified melamine formaldehyde (rGO@MF) superhydrophobic sponge for efficient oil–water separation," *Journal of Porous Materials*, vol. 25, no. 5, pp. 1475–1488, 2018.

[21] S. Sun, S. Tang, X. Chang et al., "A bifunctional melamine sponge decorated with silver-reduced graphene oxide nanocomposite for oil-water separation and antibacterial applications," *Applied Surface Science*, vol. 473, pp. 1049–1061, 2019.

[22] Z. Li, F. He, and B. Lin, "Preparation of magnetic superhydrophobic melamine sponge for oil-water separation," *Powder Technology*, vol. 345, pp. 571–579, 2019.

[23] H. Wang, J. Yang, X. Liu, Z. Tao, Z. Wang, and R. Yue, "A robust 3D superhydrophobic sponge for *in situ* continuous oil removing," *Journal of Materials Science*, vol. 54, no. 2, pp. 1255–1266, 2019.

[24] L. Li, B. Li, J. Dong, and J. Zhang, "Roles of silanes and silicones in forming superhydrophobic and superoleophobic materials," *Journal of Materials Chemistry A*, vol. 4, no. 36, pp. 13677–13725, 2016.

[25] Z. Lei, G. Zhang, Y. Ouyang, Y. Liang, Y. Deng, and C. Wang, "Simple fabrication of multi-functional melamine sponge," *Materials Letters*, vol. 190, pp. 119–122, 2017.

[26] Y. Xiang, Y. Pang, X. Jiang, J. Huang, F. Xi, and J. Liu, "One-step fabrication of novel superhydrophobic and superoleophilic sponge with outstanding absorbency and flame-retardancy for the selective removal of oily organic solvent from water," *Applied Surface Science*, vol. 428, pp. 338–347, 2018.

[27] L. Zhang, H. Li, X. Lai, X. Su, T. Liang, and X. Zeng, "Thiolated graphene-based superhydrophobic sponge for oil-water separation," *Chemical Engineering Journal*, vol. 316, pp. 736–743, 2017.

[28] V. H. Pham and J. H. Dickerson, "Superhydrophobic silanized melamine sponge as high efficiency oil absorbent materials," *ACS Applied Materials & Interfaces*, vol. 6, no. 16, pp. 14181–14188, 2014.

[29] E. Yilgör and I. Yilgör, "Silicone containing copolymers: synthesis, properties and applications," *Progress in Polymer Science*, vol. 39, no. 6, pp. 1165–1195, 2014.

[30] J. Peng, J. Deng, Y. Quan et al., "Superhydrophobic melamine sponge coated with striped polydimethylsiloxane by thiol–ene click reaction for efficient oil/water separation," *ACS Omega*, vol. 3, pp. 5222–5228, 2018.

[31] H. Zhu, S. Yang, D. Chen et al., "A robust absorbent material based on light-responsive superhydrophobic melamine sponge for oil recovery," *Advanced Materials Interfaces*, vol. 3, no. 5, p. 1500683, 2016.

[32] Z. Li, H. Wu, W. Chen, F. He, and D. Li, "Preparation of magnetic superhydrophobic melamine sponge for effective oil-water separation," *Separation and Purification Technology*, vol. 212, pp. 40–50, 2019.

[33] F. Liu and Q. Pan, "Fast and highly reversible switching of wettability through macroscopic shape change," *Journal of Materials Chemistry A*, vol. 6, no. 24, pp. 11288–11295, 2018.

[34] Z. Lei, P. Zheng, L. Niu et al., "Ultralight, robustly compressible and super-hydrophobic biomass-decorated carbonaceous melamine sponge for oil/water separation with high oil retention," *Applied Surface Science*, vol. 489, pp. 922–929, 2019.

[35] S. Pan, R. Guo, and W. Xu, "Photoresponsive superhydrophobic surfaces for effective wetting control," *Soft Matter*, vol. 10, no. 45, pp. 9187–9192, 2014.

[36] L. Li, S. Pan, E. Ou et al., "Morphological patterns of controlled particle dispersion by photoisomerization of spiropyrans," *Materials Letters*, vol. 180, pp. 291–294, 2016.

[37] H. K. Yang, A. E. Özçam, K. Efimenko, and J. Genzer, "Photochromic materials with tunable color and mechanical flexibility," *Soft Matter*, vol. 7, no. 8, pp. 3766–3774, 2011.

[38] T. Zhang, L. Fu, Z. Chen, Y. Cui, and X. Liu, "Photochromic properties of spiropyran in epoxy resin as anti-counterfeiting coating on flexible materials," *Progress in Organic Coatings*, vol. 100, pp. 100–104, 2016.

[39] Y. Yang, T. Zhang, J. Yan et al., "Preparation and photochromic behavior of spiropyran-containing fluorinated polyacrylate hydrophobic coatings," *Langmuir*, vol. 34, no. 51, pp. 15812–15819, 2018.

[40] K. Li, X. Zeng, H. Li, X. Lai, and H. Xie, "Effects of calcination temperature on the microstructure and wetting behavior of superhydrophobic polydimethylsiloxane/silica coating," *Colloids and Surfaces A: Physicochemical and Engineering Aspects*, vol. 445, pp. 111–118, 2014.